JGR Space Physics

RESEARCH ARTICLE
10.1029/2023JA031375

Significant Mid- and Low-Latitude Ionospheric Disturbances Characterized by Dynamic EIA, EPBs, and SED Variations During the 13–14 March 2022 Geomagnetic Storm

Ercha Aa[1], Shun-Rong Zhang[1], Philip J. Erickson[1], Wenbin Wang[2], Liying Qian[2], Xuguang Cai[3], Anthea J. Coster[1], and Larisa P. Goncharenko[1]

[1]Haystack Observatory, Massachusetts Institute of Technology, Westford, MA, USA, [2]High Altitude Observatory, National Center for Atmospheric Research, Boulder, CO, USA, [3]Laboratory for Atmospheric and Space Physics, University of Colorado Boulder, Boulder, CO, USA

Key Points:

- A common key driver of storm-time electric field generated three dynamic ionospheric changes simultaneously from low to subauroral latitudes
- Equatorial ionization anomaly crests showed merging and separation during interplanetary magnetic field Bz oscillation, and strong equatorial plasma bubbles reached 30° MLAT corresponding to 2,600 km Apex height
- Salient storm-enhanced density associated with subauroral polarization stream occurred in midlatitudes, showing a dynamic temporal variation that intensified and diminished twice

Correspondence to:
E. Aa,
aercha@mit.edu

Citation:
Aa, E., Zhang, S.-R., Erickson, P. J., Wang, W., Qian, L., Cai, X., et al. (2023). Significant mid- and low-latitude ionospheric disturbances characterized by dynamic EIA, EPBs, and SED variations during the 13–14 March 2022 geomagnetic storm. *Journal of Geophysical Research: Space Physics*, *128*, e2023JA031375. https://doi.org/10.1029/2023JA031375

Received 4 FEB 2023
Accepted 11 JUL 2023

Abstract This work investigates mid- and low-latitude ionospheric disturbances over the American sector during a moderate but geo-effective geomagnetic storm on 13–14 March 2022 (π-Day storm), using ground-based Global Navigation Satellite System total electron content data, ionosonde observations, and space-borne measurements from the Global-scale Observations of Limb and Disk (GOLD), Swarm, the Defense Meteorological Satellite Program (DMSP), and the Ionospheric Connection Explorer (ICON) satellites. Our results show that this modest but geo-effective storm created a number of large ionospheric disturbances, especially the dynamic multi-scale electron density gradient features in the storm main phase as follows: (a) The low-latitude equatorial ionization anomaly (EIA) exhibited a dramatic storm-time deformation and reformation, where the EIA crests evolved into a bright equatorial band for 1–2 hr and then quickly separated back into the typical double-crest structure with a broad crest width and deep equatorial trough. (b) Strong equatorial plasma bubbles (EPBs) occurred with an abnormally high latitude/altitude extension, reaching the geomagnetic latitude of ∼30°, corresponding to an Apex height of 2,600 km above the dip equator. (c) The midlatitude ionosphere experienced a conspicuous storm-enhanced density (SED) plume structure associated with the subauroral polarization stream (SAPS). This SED/SAPS feature showed an unusual temporal variation that intensified and diminished twice. These distinct mid- and low-latitude ionospheric disturbances could be attributed to the storm-time electrodynamic effect of electric field perturbation, along with contributions from neutral dynamics and thermospheric composition change.

1. Introduction

The morphology and variation of two important low-latitude ionospheric phenomena with large density gradients, the equatorial ionization anomaly (EIA) and equatorial plasma bubbles (EPBs), have been the focus of major research efforts for decades. This is due to their adverse effects on radio waves used for navigation and communication systems (Eastes et al., 2019). The EIA manifests as two enhanced plasma density crests around ±15° geomagnetic latitudes and an equatorial density trough, which is caused by the so-called "fountain effect" through a combination of upward equatorial E × B drift and ambipolar diffusion due to pressure gradient and gravity (Appleton, 1946; Duncan, 1960). EIA crests are some of the most significant density enhancement structures in the global ionosphere, developing in the daytime and continuing to manifest through the evening hours (Balan et al., 2018). In contrast, EPBs refer to structures of irregular plasma density depletion with various scales (a few tens to hundreds of km in the zonal direction) that are generated via the Rayleigh-Taylor instability in the nighttime equatorial ionosphere with a steep vertical density gradient after the E-region decays. EPBs can be usually observed between EIA crests from the bottomside F region to topside altitudes of ∼1,000 km (e.g., Kelley et al., 1976; Woodman & La Hoz, 1976). The most dramatic variation of EIA and development of EPBs occur in the postsunset hours. During this period, the prereversal enhancement (PRE) of the eastward electric field increases upward plasma drift in the equatorial region. This not only uplifts the ionosphere to higher altitudes, reducing chemical loss and maintaining EIA, but also destabilizes the bottomside F layer by increasing the growth rate of the Rayleigh-Taylor instability and thus favoring the occurrence of EPBs (e.g., Abdu et al., 1982; Fejer et al., 1999).

The midlatitude ionosphere is also an important interface in the global ionospheric dynamic system. It is subject to variable energy and momentum inputs from the auroral/polar latitudes and may also be influenced by the

expanded dynamic low-latitude EIA/EPBs perturbations during intense storms. Like the low-latitude ionosphere, the midlatitude ionosphere can also exhibit prominent density gradient structures, especially under geomagnetically active conditions, such as the storm-enhanced density (SED, Foster, 1993). SED refers to large-scale midlatitude electron density or total electron content (TEC) enhancement in the local afternoon and dusk sector during storm early stages, which is usually characterized by a spatially narrow but distinct "plume" structure along a highly variable sunward/poleward plasma convection channel at mid- and subauroral latitudes that extends from a high-density "base" area in the lower mid-latitude and poleward of the EIA crest (e.g., Coster et al., 2007; Foster et al., 2021; Zhang & Aa, 2021; Zou et al., 2013). SED was initially considered as a "dusk effect" or regional ionospheric positive storm effect during the storm main phase (Buonsanto, 1999; Mendillo, 2006). With the growing availability of Global Navigation Satellite Systems (GNSS) data and various ground-based and space-borne measurements, SED understanding evolved to become part of a larger set of interconnected geospace storm processes, likely associated with the expansion of high-latitude convection pattern (Heelis et al., 2009; Thomas et al., 2013), erosion of the outer plasmasphere (Moldwin et al., 2016; Yizengaw et al., 2006), and the occurrence of subauroral polarization stream (SAPS) electric fields (Foster & Burke, 2002).

During geomagnetic storms, the mid- and low-latitude ionosphere-thermosphere system undergoes large disturbances due to electrodynamics, dynamics, and composition variations, which can generate significant changes in the storm-produced ionospheric electron density structures. In particular, the low and mid-latitude zonal electric field can be modified drastically by the prompt penetration of high-latitude electric field due to rapidly varying magnetospheric convection (e.g., Fejer, 2002; Heelis, 2004; C.-S. Huang et al., 2007; Kikuchi et al., 1978), and by the disturbance dynamo electric field due to changes of the thermospheric neutral wind pattern that often become dominant a few hours after the storm onset, especially in the recovery phase (e.g., Blanc & Richmond, 1980; Fuller-Rowell et al., 2002; Maruyama et al., 2005; Scherliess & Fejer, 1997). Thus, the storm-time low-latitude ionospheric electrodynamic processes can greatly affect the morphology and intensity of EIA through the modified fountain effect (e.g., Astafyeva et al., 2018; Balan et al., 2009; Luan, 2021). For instance, the penetration electric field, with eastward polarity in the daytime through evening hours, may cause a large uplift of the equatorial ionosphere and strong ambipolar plasma diffusion, creating a "super-fountain" effect with enhanced and broadened EIA crests (Lin et al., 2005; Mannucci et al., 2005; Tsurutani et al., 2004). The storm-time electrodynamic effect can also play an essential role, increasing or suppressing the development of EPBs depending on the polarity of penetration and disturbance dynamo electric field at different local time sectors and storm phases. In the dusk sector, the eastward penetration electric field can be superimposed on the PRE, leading to a larger upward plasma drift that is favorable for the Rayleigh-Taylor instability growth (e.g., Aa et al., 2019; Tulasi Ram et al., 2008; Zakharenkova et al., 2019). In comparison, the disturbance dynamo is westward through the day and dusk sector but eastward at night and dawn. This can suppress EPBs before midnight, although this condition may sometimes promote postmidnight EPBs occurrence (e.g., Carter et al., 2016; Li et al., 2009; Yeh et al., 2001). In the mid-latitude ionosphere, from the dayside through the dusk sector, local upward $E \times B$ drift due to eastward penetration electric field leads to enhanced plasma density that facilitates the development of SED structures (e.g., David et al., 2011; Deng & Ridley, 2006; Heelis et al., 2009; Liu et al., 2016; Zou et al., 2014).

Besides electrodynamics effects, the mid- and low-latitude ionosphere electron densities change in response to storm-time neutral dynamics and composition variations. The storm-time equatorward neutral wind surge raises the ionosphere to higher altitudes with a slower chemical loss rate, producing positive ionospheric storm effects that strengthen the EIA crests at low latitudes and contribute to the uplift and formation of SED at midlatitudes (e.g., Anderson, 1976; Balan et al., 2010; Datta-Barua et al., 2011; Lu et al., 2008; W. Wang et al., 2021). In addition, the magnetic meridional/trans-equatorial neutral winds act to increase the field line-integrated conductivity so that the equatorial Rayleigh-Taylor growth rate and EPBs could be somewhat suppressed, though this effect is much weaker than the dominant electrodynamics effect from PRE and storm-disturbed electric field (Abdu, 2019; Sultan, 1996). Last but not least, thermospheric composition changes due to the altered global circulation also play a role in causing negative/positive ionospheric disturbances. The neutral density ratio O/N_2 is reduced via atmospheric upwelling of nitrogen-rich air through constant pressure surfaces at high latitudes that are transported to mid and low latitudes by equatorward winds and/or traveling atmospheric disturbances (TADs), while the O/N_2 is increased via downwelling of atomic oxygen at lower latitudes equatorward of the composition disturbance zone (Prölss, 1980, 2011). Given that the ionosphere is typically raised to high altitudes by equatorward neutral winds via dynamic effect as well as by the penetration electric fields via electrodynamic effect during the early stages of a storm, the composition effect can be more effective and trigger midlatitude negative

ionospheric storm effects during the recovery phase (Fuller-Rowell et al., 1994; Prölss, 2008). The combination and interaction of different storm-time effects make mid- and low-latitude ionosphere structures exhibit very complicated and dynamic variations.

During the past Solar Cycles 23 and 24, our understanding of the storm-time mid- and low-latitude ionosphere disturbances, especially the behavior of multi-scale electron density gradient structures, has been greatly advanced through extensive studies on several intense geospace storm events. These include but are not limited to the Halloween Storm on 29–30 October 2003 (minimum Dst index of −383 nT) and the super storm on 20–21 November 2003 (minimum Dst index of −422 nT) (e.g., Basu et al., 2007; Foster & Rideout, 2005; Gardner et al., 2018; Kil et al., 2006; Lin et al., 2005; Mannucci et al., 2005; Zhao et al., 2005), the St. Patrick's day storms during 17–18 March in 2013 (minimum Dst index of −132 nT) and 2015 (minimum Dst index of −223 nT) (e.g., Carter et al., 2016; Ferdousi et al., 2019; Huba et al., 2017; Liu et al., 2016; Nava et al., 2016; Zakharenkova et al., 2019; Zhang et al., 2017), the storm on 22–23 June 2015 (minimum Dst index of −204 nT) (e.g., Astafyeva et al., 2018; Singh & Sripathi, 2017), the storm on 07–08 September 2017 (minimum Dst index of −142 nT) (e.g., Aa et al., 2018; Aa et al., 2019; Mrak et al., 2020; Nishimura et al., 2021; Qian et al., 2019; Z. Wang et al., 2021; Zakharenkova & Cherniak, 2020; Zhang et al., 2019), and the storm on 25–26 August 2018 (minimum Dst index of −174 nT) (e.g., Astafyeva et al., 2022; Chang et al., 2022; Cherniak & Zakharenkova, 2022; Spogli et al., 2021; Zhang et al., 2022).

Despite remarkable progress that has been achieved through prior storm studies over the past decades, there still remain some important issues that need to be further addressed to achieve a better understanding of storm-time mid- and low-latitude responses: (a) The variation and interaction of major drivers for each storm can be quite unique and complex, making it difficult to explain the dynamic ionospheric spatial-temporal evolution of different storms with a unified interpretation. In particular, a moderate storm or even minor geomagnetic forcing during the so-called "weak/quiet" geomagnetic conditions around a solar minimum can still be quite geo-effective and trigger salient ionospheric and thermospheric disturbances (Aa et al., 2021; Cai, Burns, Wang, Qian, Pedatella, et al., 2021; Cai et al., 2020; Zhai et al., 2023). With the increase of solar activity out of minimum in Solar Cycle 25, it is important to monitor and investigate the latest storm-time ionospheric response in the ascending phase of the solar cycle and compare it with historic events mainly from solar maximum and declining phases of previous solar cycles. (b) The storm-time mid- and low-latitude ionosphere can exhibit far more complicated electron density perturbation structures than might otherwise be expected, such as SED, EIA, and EPBs. However, these density perturbation structures with large gradients are often viewed separately with few global contexts, which naturally raises questions to be answered, such as: Can the storm-time variation of different density structures be explained by a common driver? Is there an interaction between the dynamic evolution of structures in different regions? Thus, understanding the storm-time variability and underlying mechanism of these different but related ionospheric perturbation structures remains an important perspective for storm science. (c) Lacking of observational data is still a critical issue, especially for low-latitude multi-sensor ionospheric studies. Besides the ever-growing ground-based GNSS network and the pre-established space-borne instruments, some recently launched satellite missions, such as the Global-scale Observations of the Limb and Disk (GOLD) and the Ionospheric Connection Explorer (ICON), provide new observational abilities that help to better understand the storm-time ionospheric/thermospheric responses in Solar Cycle 25.

Therefore, in the current paper, we investigate a moderate but quite geo-effective geomagnetic storm that occurred on 13–14 March 2022 in the ascending phase of ongoing solar cycle 25, utilizing multi-instrument data from ground-based GNSS receivers and ionosondes, as well as space-borne measurements from several satellite missions including GOLD, ICON, Swarm, and DMSP. The main focus is to analyze mid- and low-latitude ionospheric disturbances over the American sector, especially the behavior of multi-scale electron density structures and their underlying mechanisms. In particular, we found a series of distinct storm-time characteristics in different regions. These include (a) deformation and reformation of EIA crests, which evolved into a broad single equatorial band and separated back into a double-crest structure in 2 hr during the main phase. Although storm-time single-peak EIA structures were reported during the recovery phase (e.g., Basu et al., 2009; C. M. Huang et al., 2010; Sreeja et al., 2009), such a dynamic EIA merging and separation during the storm main phase is rarely reported. (b) abnormally high-latitude/altitude EPBs that reached a geomagnetic latitude of ∼30° and Apex height of 2,600 km. Considering EPBs are usually observed below 1,000 km altitude (Kelley et al., 1976; Woodman & La Hoz, 1976), such a high-latitude/altitude extension of storm-time EPBs is considered as an unusual phenomenon (Sousasantos et al., 2023). (c) A salient temporal variation of midlatitude SED structure

that was intensified and diminished twice associated with SAPS. The coordinated in-depth analysis of these features and their possible drivers motivated this study, which provides a new understanding of storm-time variations and interactions of mid- and low-latitude electrodynamics and neutral dynamics.

2. Instruments and Data Description

Ground-based GNSS TEC data deriving from 5,000+ worldwide receivers (with 3,000+ from the American sector) are routinely produced at the Massachusetts Institute of Technology's Haystack Observatory. Gridded TEC products are distributed to the community with a spatial resolution of 1° (longitude) by 1° (latitude) and a time cadence of 5 min (Rideout & Coster, 2006; Vierinen et al., 2016). We also utilize the differential TEC (dTEC) to examine storm-time TIDs, which are derived by removing the background trend for all satellite-receiver line-of-sight TEC pairs via a Savitzky-Golay low-pass filter algorithm with a 30-min sliding window (Savitzky & Golay, 1964; Zhang et al., 2019). Besides GNSS TEC, four ionosonde measurements in the American sector from the equatorial to subauroral latitudes are used to explore storm-time electrodynamics and irregularity features, including Fortaleza (3.9°S, 38.4°W), Ramey (18.5°N, 67.1°W), Millstone Hill (42.6°N, 71.5°W), and Alpena (45.1°N, 83.6°W).

The GOLD ultraviolet spectrometers image the terrestrial ionosphere and thermosphere in a geostationary orbit at 47.5°W longitude with the merit of unchanged field of view, measuring Earth's airglow emissions between 134 and 160 nm through the disk, limb, and stellar occultation (Eastes et al., 2017, 2020). In this study, we use the nighttime 2-D disk images of OI 135.6 nm emission that is proportional to the square of F-region peak density. GOLD provides continuous time-evolving maps in the early evening hours to unambiguously reveal the spatial-temporal variation of EIA and EPB structures from West Africa to America (e.g., Aa et al., 2020, 2022, 2023; Cai, Burns, Wang, Qian, Liu, et al., 2021; Cai et al., 2022, 2023; Eastes et al., 2019). Moreover, we also use the GOLD column density ratio of O/N_2 to analyze the thermospheric composition variations, which is derived from the daytime disk measurements of OI 135.6 nm and the N_2 Lyman-Birge-Hopfield (LBH) emission (Strickland et al., 1995).

We also use space-borne measurements from the following three low-Earth orbiting satellite missions: ICON, Swarm, and the Defense Meteorological Satellite Program (DMSP). ICON flies at an altitude of 575 km with an inclination angle of 27° for mid- and low-latitude ionospheric and thermospheric measurements (Immel et al., 2018). In this study, we use thermospheric neutral wind data from the Michelson Interferometer for Global High-Resolution Thermospheric Imaging (MIGHTI) instrument (Harding et al., 2017). The Swarm constellation includes three identical polar-orbiting satellites at an inclination angle of ∼88°, with Swarm A and C flying side-by-side with a longitudinal separation of 1.4° at ∼450 km and Swarm B flying at ∼510 km (Friis-Christensen et al., 2008). Additionally, we use the electron density data from the electric field instrument onboard Swarm satellites. The DMSP constellation flies in a sun-synchronous polar orbit at an altitude of ∼850 km. We use the ion density and cross-track plasma drift data from the ionospheric plasma monitor sensor as well as the electron and ion energy flux data from the precipitating particle sensor.

3. Interplanetary and Geomagnetic Conditions

Figure 1 shows temporal variations of solar wind speed and dynamic pressure, interplanetary magnetic field (IMF) By and Bz components, Interplanetary electric field (IEF) By component, planetary K-index (Kp), and the longitudinally symmetric index (SYM-H) between March 13–15, 2022. Solar activity was at a moderate level with the F10.7 solar radio flux ranging between 121 and 109 SFU (1 SFU = 10^{-22} W/m^2/Hz). On March 13, a coronal mass ejection (CME) arrived at the Earth at around 11 UT, with the solar wind velocity increasing sharply from 350 km/s to 550 km/s and then gradually settling at ∼480 km/s at the end of March 13. The IMF Bz became highly volatile and experienced one moderate southward excursion around 12–14 UT as well as two large southward dips around 16–18 UT and 22–23:30 UT with a minimum negative value of −26.5 nT at 22:45 UT. The SYM-H index also exhibited consecutive dips following the IMF Bz disturbance after the sudden commencement on March 13, which reached a minimum value of −113 nT at 23:40 UT and gradually recovered on March 14. The Kp index reached 6- at 12 UT on March 13 and slightly fluctuated between 5+ and 6+ until 03 UT on March 14. This storm was only classified as a G2 (moderate) storm based on the National Oceanic and Atmospheric Administration (NOAA) space weather scales (https://www.swpc.noaa.gov/noaa-scales-explanation). However, Kp may not always be a sufficient proxy to characterize a storm's effects, and additional parameters such as the

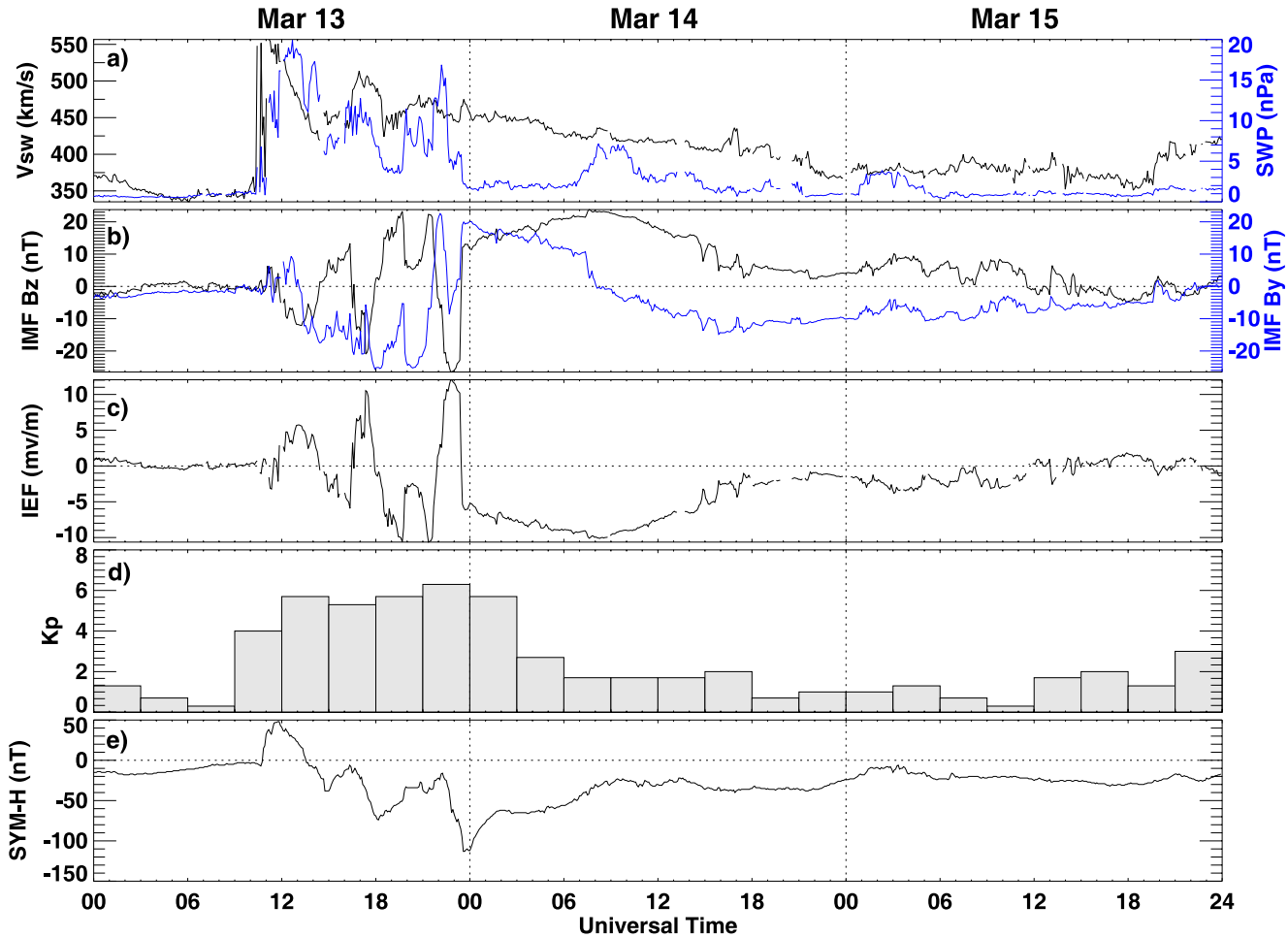

Figure 1. Temporal variations of (a) solar wind speed and dynamic pressure, (b) interplanetary magnetic field (IMF) By and Bz, (c) interplanetary electric field (IEF) By component, (d) Kp index, and (e) longitudinally symmetric index (SYM-H) during March 13–15, 2022.

interplanetary magnetic field should also be considered. In this storm, the above-mentioned IMF Bz variation and associated penetration electric fields created a series of distinct mid- and low-latitude ionospheric disturbances over the American sector, which will be described and discussed below.

4. Results

Figures 2a–2c show three maps that combine GNSS TEC and GOLD OI 135.6 nm radiance images at 21:22 UT, 22:52 UT, and 00:10 UT on March 13–14, respectively. These provide synoptic glimpses of the mid- and low-latitude ionospheric morphology during the storm main phase over the American-Atlantic longitude sector. Figures 2d–2f show the corresponding quiet time results from the previous day as a reference. As can be seen, the storm-time mid- and low-latitude ionosphere exhibited significant differences both in morphology and magnitude compared to quiet-time results. At 21:22 UT (Figure 2a), the storm-time mid-latitude ionosphere in both hemispheres was registered with a considerable positive storm effect, with TEC values being enhanced by 15–25 TEC unit (TECU) (~30%–50%) with respect to quiet time values. In particular, the GNSS TEC and GOLD radiance values peaked in the equatorial region with no clear double-crest structure but exhibited a single equatorial bright band slightly southward of the dip equator. In contrast, the EIA on the reference quiet day (Figure 2d) showed typical double crests around ±15° geomagnetic latitude (MLAT).

At 22:52 UT (Figure 2b), the previous storm-time equatorial band was clearly replaced by two EIA crests, which manifested as double bright low-latitude arcs with a shallow equatorial density trough in between near the magnetic equator shown by the GOLD image. Moreover, compared to quiet time crests location around 15–20°

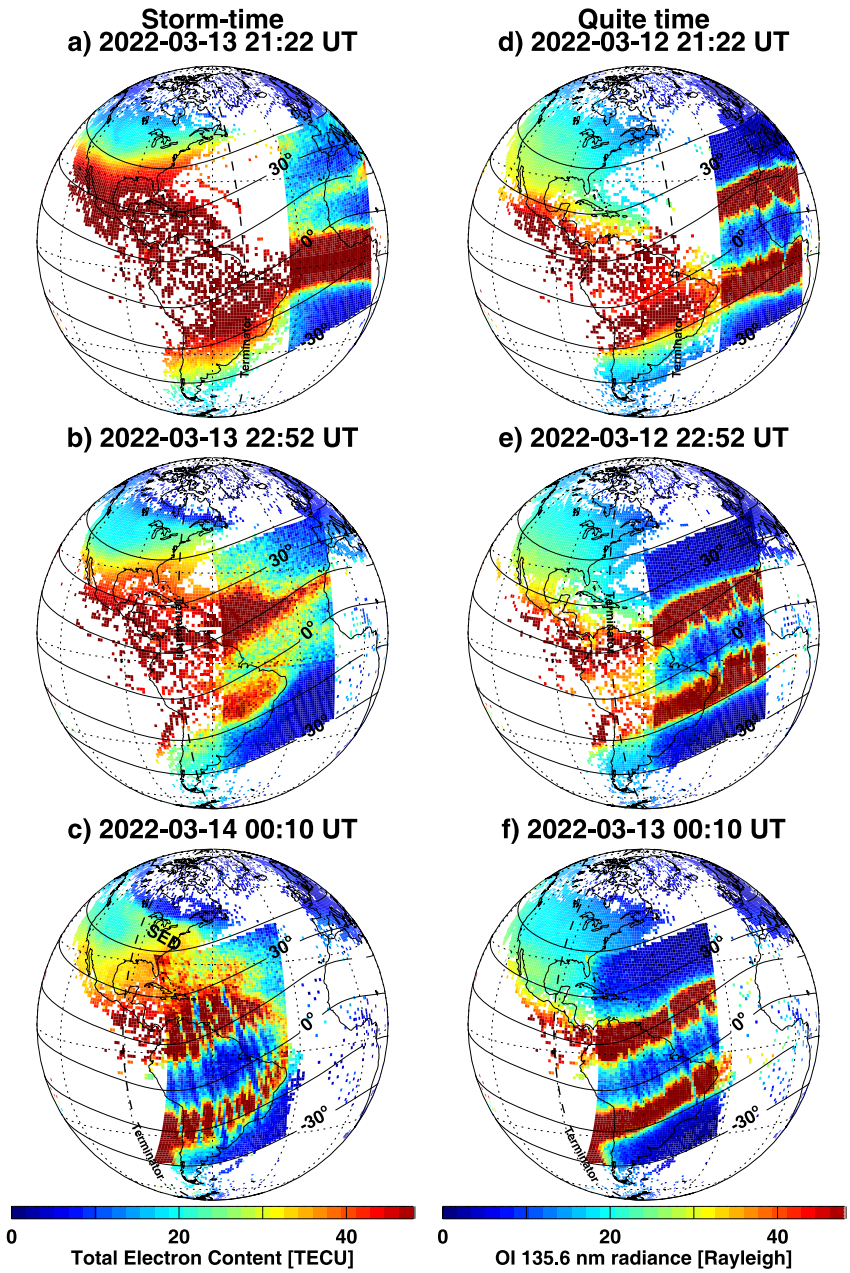

Figure 2. Combined GNSS TEC and GOLD OI 135.6-nm radiance maps at three UTs during (a–c) the storm time on March 13–14 and (d–f) the previous day as the quiet time reference, respectively. The sunset terminator and geomagnetic latitudes with 15° interval are also shown.

MLAT (Figure 2e), the storm-time northern EIA crest was significantly broadened, especially in the poleward directions, occupying a much wider latitudinal range of 10–30° MLAT. For example, the poleward edge of EIA northern crest at 60° W longitude was around 20° MLAT in quiet time, while it was expanded to 30° MLAT at the same longitude during storm time. This dynamic EIA variation from merging to separation and broadening occurred within a short time interval of ~90 min. Such a feature has rarely been reported in previous ionospheric storm studies.

At 00:10 UT (Figure 2c), significant EPB structures that manifest as multiple parallel dark streaks appeared in the equatorial trough, suggesting rapid development of Rayleigh-Taylor instability possibly due to large equatorial upward plasma drift through the combination of postsunset PRE and storm-time penetration electric field (e.g.,

Kil et al., 2006; Shiokawa et al., 2004). Although EPBs also occurred during the previous quiet time evening sector since 21:22 UT as shown in Figures 2d–2f, one important difference is that the storm-time plasma bubbles showed a much faster development with considerable latitudinal extension that cut through the broadened EIA crests and even reached as high as 30° MLAT, which corresponds to an Apex altitude of ∼2,600 km above the dip equator. Such a high-latitude/altitude extension of storm-time EPBs is much stronger than their quiet-time counterparts that reach ∼15–18° MLAT (∼1,000 km Apex altitude (cf., Figures 2d–2f).

Moreover, the northern EIA crest in Figure 2c extended further northward toward the Florida and Caribbean area around 35° MLAT, showing an anomalously large electron density gradient therein, similar to the so-called "Florida effect" that refers to anomalously large TEC enhancements (as large as several tens of TEC unit) to the north of EIA crest around the Florida coast (Foster & Coster, 2007). Moreover, a noticeable midlatitude SED feature can be observed in the local dusk over the continental US. This was characterized by a plume-like TEC enhancement structure that stemmed from the large electron density base area in the poleward edge of EIA crest and extended in the northwestward direction to the dayside. Taken as a whole, these consecutive occurrences of dynamic deformation and reformation of EIA crests, extreme poleward-extending high-altitude EPBs, and a strong SED feature potentially associated with the Florida effect, to the best of our knowledge, are notable and have rarely been simultaneously observed in a moderate storm before. Their characteristics will be further investigated in this study.

4.1. Deformation and Reformation of EIA Crests

We first investigate the EIA deformation and reformation by utilizing both ground-based observations and space-borne measurements from low-Earth and geostationary orbits. Figure 3 shows maps combining GNSS TEC and GOLD OI 135.6 nm radiance images over the American-Atlantic longitude sector with overlapping consecutive Swarm B (blue) and Swarm C (red) satellite orbits at four intervals on March 13. At 19:10 UT (Figure 3a), the double-crest EIA morphology was discernible in the GNSS TEC map and can be clearly identified in Swarm electron density latitudinal profiles. Taking Swarm C that flew at a slightly lower altitude of ∼450 km as an example, the peak magnitude of EIA crests was around $1.7 \times 10^6/cm^3$, while the density of the equatorial trough was around $0.8–0.9 \times 10^6/cm^3$. Thus the crest-to-trough ratio of EIA is around 2 at this time. However, at 20:52 UT (Figure 3b), GOLD observed a merely single bright equatorial band in the early evening sector, and there was no double-crest feature in the GNSS TEC map but rather an enhanced equatorial peak. In the Swarm C latitudinal profile, the previous equatorial trough was also replaced by a flattened equatorial curve. At 22:10 UT (Figure 3c), the EIA latitudinal profiles from Swarm observations transformed into a Mesa-type morphology similar to a flattened-top hill, with the crests remaining less changed while the trough region being filled with plasma. The crest-to-trough ratio was around 1. At 23:52 UT (Figure 3d), significant EIA crests and pronounced equatorial trough reformed as can be seen from both 2-D images and 1-D electron density latitudinal profiles, with the EIA crest-to-trough ratio being increased to ∼3. Moreover, the crests' peak location in Swarm profiles also exhibited considerable latitudinal variation. Taking the southern crest in Swarm C as an example, the peak MLAT location was changed from 13°S at 19:10 UT to 10°S at 20:52 UT, then to 5°S at 22:10 UT, and then back to 13°S at 23:52 UT.

To better trace the merging and separation of EIA crests, Figure 4 presents twelve consecutive images of GNSS TEC and GOLD nighttime OI 135.6 nm radiance showing the continuous EIA evolution over the American-Atlantic sector during 20:10–22:52 UT on March 13. The EIA double-crests were noticeable at 20:10 UT (Figure 4a) and 20:22 UT (Figure 4b). Nevertheless, starting from 20:40 UT (Figure 4c), the postsunset double EIA crests, especially the northern one, rapidly collapsed toward the equator while merging together around the West African area. They formed into one bright equatorial band over the Atlantic sector and continued for 60–80 min (Figures 4d–4h). However, starting from 22:25 UT (Figure 4j), the bright equatorial band gradually separated into double EIA crests. The previous high-density equatorial peak was replaced by an equatorial trough, and the restored northern EIA crest expanded to a wide latitudinal range of 10–30° MLAT. This suggests considerable removal of equatorial plasma possibly associated with the storm-enhanced fountain effect, considering that the equatorial TEC and OI radiance was decreased by more than 50% compared with the EIA-merging periods. The possible underlying mechanism of such a dynamic EIA deformation and reformation phenomenon will be analyzed in the Discussion section (Section 5).

4.2. Development of Extreme Poleward-Extending EPBs

The initiation and development process of extreme storm-time EPBs can be seen in Figure 5. At 23:10 UT (Figure 5a), the equatorial trough between the EIA crests was considerably deepened, with the plasma density

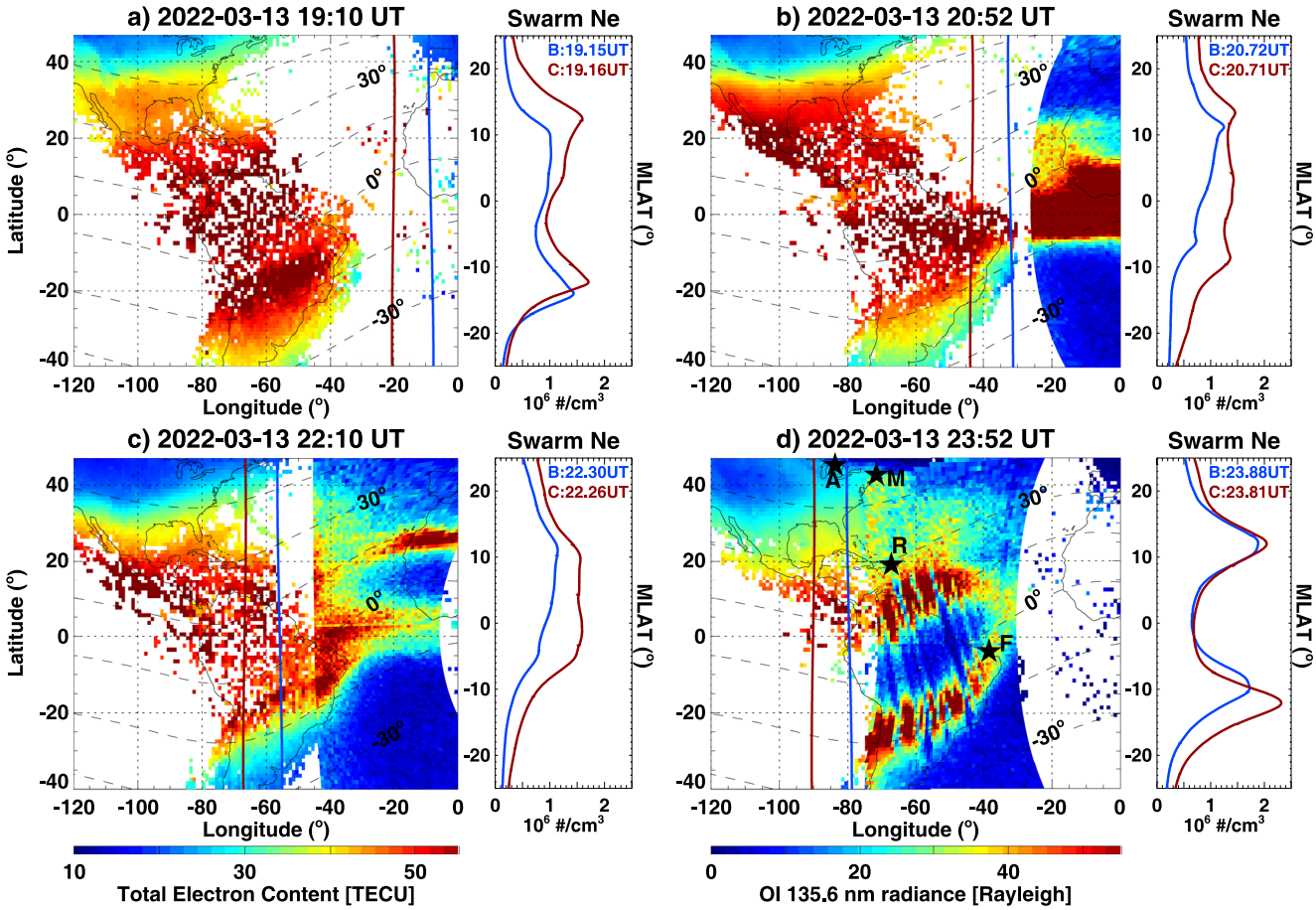

Figure 3. (a–d) GNSS TEC and GOLD OI 135.6 nm radiance (when available) maps over the American-Atlantic longitude sector with overlapping Swarm B (blue) and Swarm C (red) paths at four UTs between 19:10 UT and 23:52 UT on 13 March 2022. The geomagnetic latitudes with 15° interval are marked by the dashed lines. The black stars in panel (d) mark the location of four ionosondes: Fortaleza (F), Ramey (R), Millstone Hill (M), and Alpena (A). The right sub-panels show the electron density profiles as a function of geomagnetic latitudes along Swarm paths around 18 LT.

therein being depleted by ∼50% in 1 hr. At 23:22 UT (Figure 5b), in response to the continuous penetration electric field effect with IMF Bz below −20 nT for more than one hour, noticeable EPB signatures were seen in the equatorial trough region. In the following time intervals, these EPBs quickly formed into parallel wedge-like structures along the field lines which cut through the EIA crests. They extended to low-latitude regions and even reached 30° MLAT at 00:10 UT (Figure 5e) and 00:22 UT (Figure 5f) as previously mentioned. Moreover, the northern EIA crest occupied a wide latitude range of 10–35° MLAT during this time period, associated with large density gradients at its poleward edge and simultaneous midlatitude SED phenomena. Although there were no GOLD nighttime disk measurements after 00:22 UT, the characteristics of fully developed EPBs and broadened EIA crests can still be seen in GNSS TEC observations for the following several hours.

Recall from Figure 3d that extreme EPB signatures were not only prevalent over the Fortaleza ionosonde in the equatorial area but also extended to the lower midlatitude area around the Ramey ionosonde. We thus investigate the ionograms from these two digisondes to examine spread-F characteristics. Figure 6 displays a sequence of ionograms at Fortaleza (red) between 23:40–00:50 UT on March 13–14 and at Ramey (blue) between 00:00–01:45 UT on March 14. As can be seen, both stations exhibited significant range-type spread-F, which are typical signatures of large-scale ionospheric irregularities in the F region. At the equatorial station of Fortaleza, the diffuse echoes started to appear around 23:50 UT and quickly spread across the bottomside F region in the following intervals. This range-type equatorial spread-F is usually indicative of EPBs created at the bottomside F region via the Rayleigh-Taylor instability (Abdu, 2001). By comparison, strong spread-F echoes appeared at a later time at the lower-midlatitude Ramey station around 00:15 UT and quickly spread across the whole F region with large diffuseness near the F2 region critical frequency. Considering that Ramey ionosonde is located close

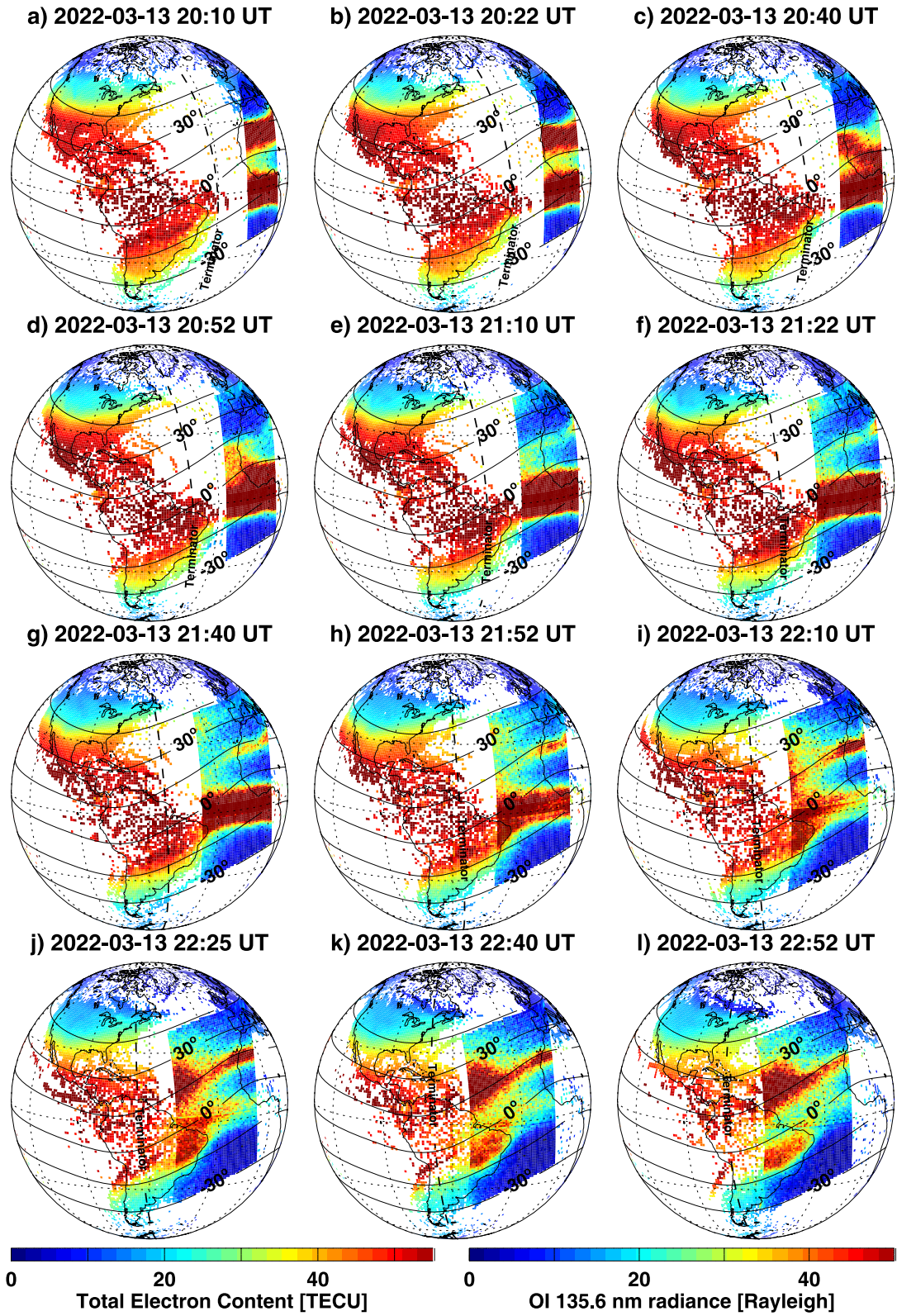

Figure 4. (a–l) Temporal variation of combined GNSS TEC and GOLD OI 135.6-nm radiance maps between 20:10 UT and 22:52 UT on March 13. The sunset terminator and geomagnetic latitudes with 15° interval are also shown.

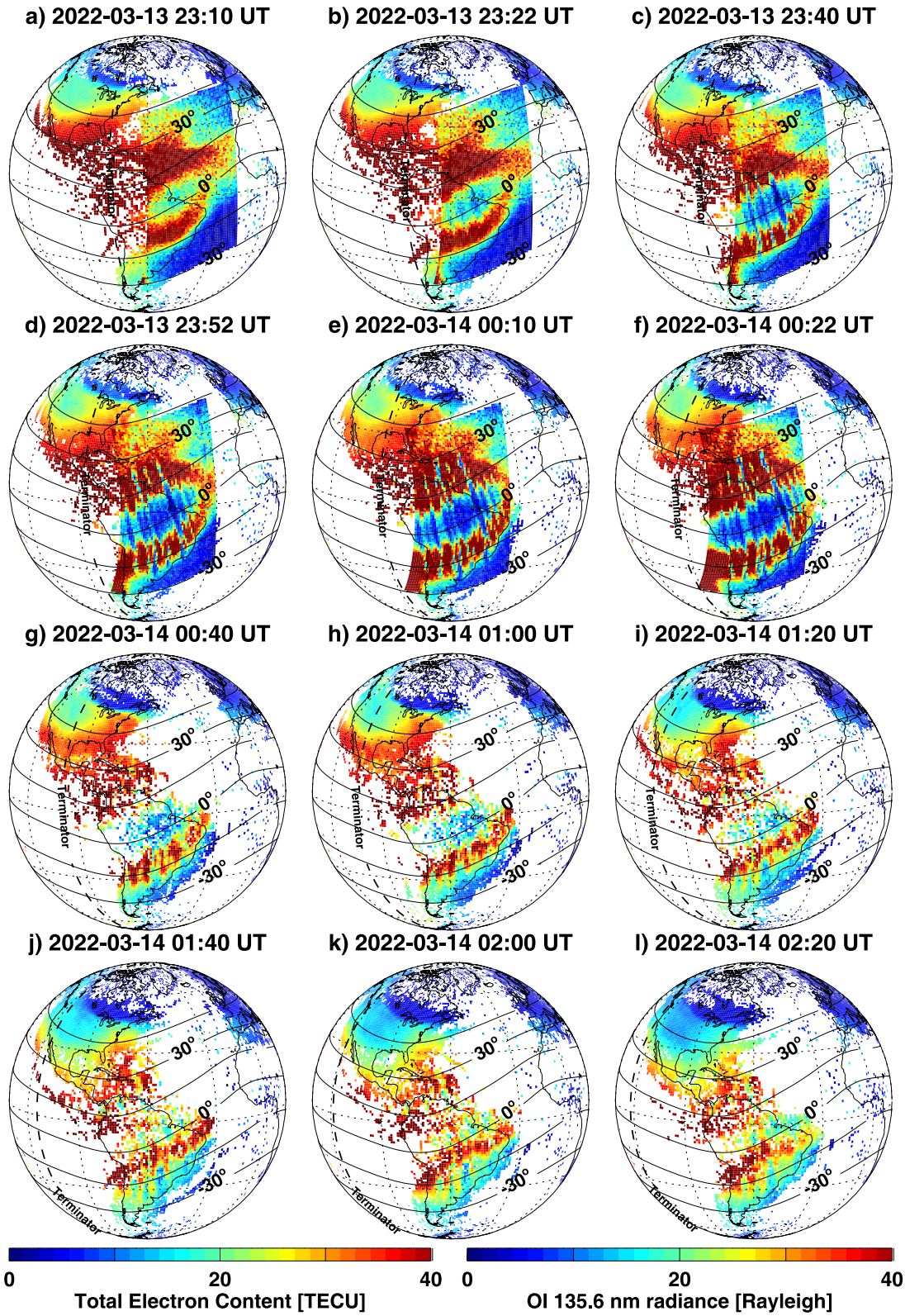

Figure 5. The same as Figure 4, but for time periods between 23:10 UT on March 13 and 02:20 UT on March 14. Note that GOLD had no nighttime observation after 00:22 UT.

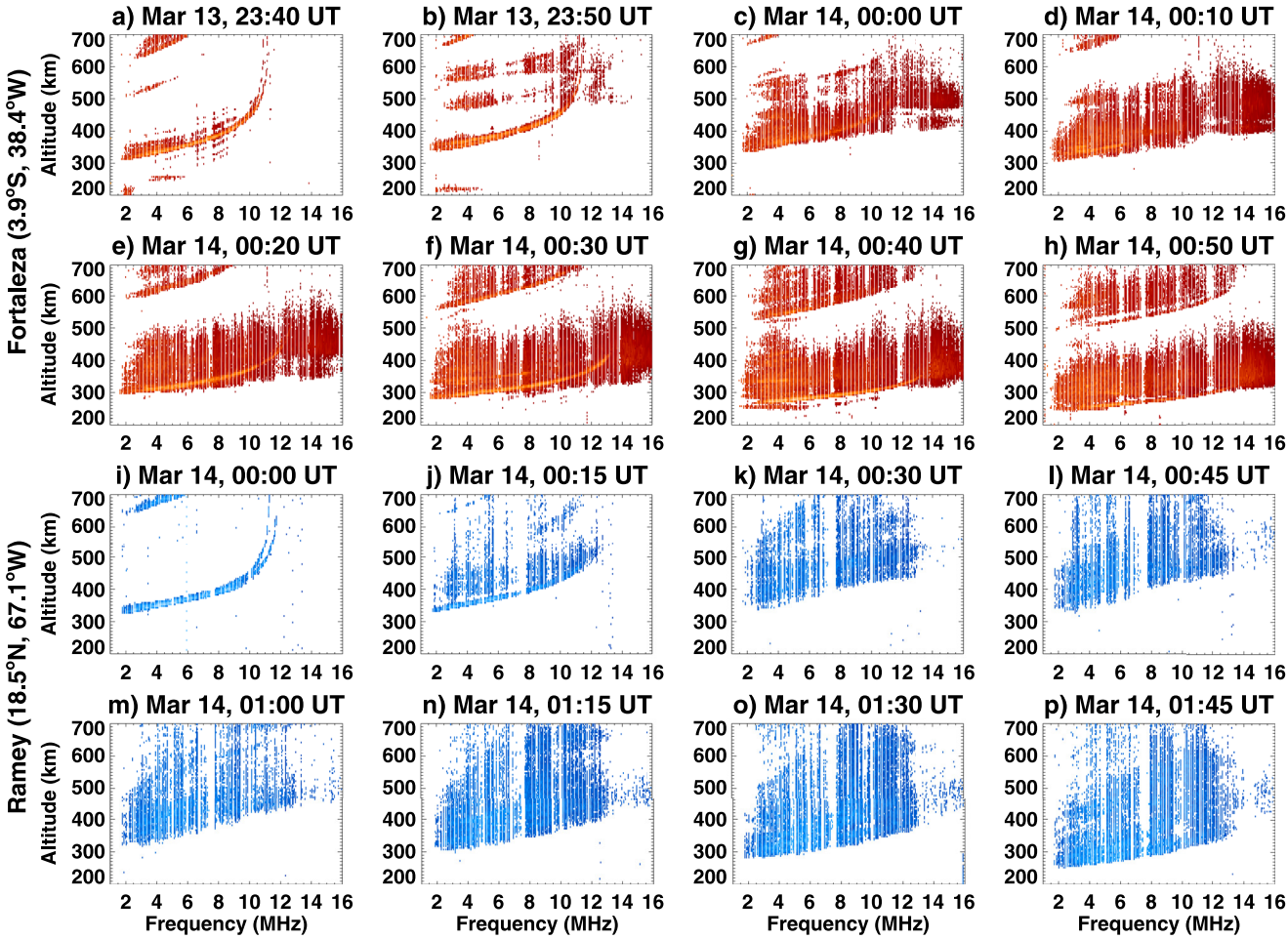

Figure 6. (a–h) Ionograms at Fortaleza station during 23:40–00:50 UT on March 13-14, 2022. (i–p) Ionograms at Ramey station during 00:00–01:45 UT on 14 March 2022.

to 29° MLAT, the range-type spread-F irregularities that occurred at this latitude in the F-region corresponded to EPBs rising to an Apex altitude of around 2,600 km above the dip equator, which is consistent with bubble estimates from GOLD 135.6 nm radiance and GNSS TEC observations. We will further investigate the mechanism of these extreme high-altitude/latitude EPBs in the Discussion section (Section 5).

4.3. Dynamic Midlatitude Ionosphere-Thermosphere Variation

As previously demonstrated in Figures 2 and 5, midlatitude SED feature was observed over the North American sector after 23 UT on March 13, characterized by a plume-like TEC enhancement that elongated northwestward toward dayside subauroral latitudes. To further examine the SED evolution and the associated subauroral plasma flow characteristics, Figures 7 and 8 show the TEC polar view using magnetic local time and geomagnetic latitude coordinates over the Northern Hemisphere, superposing DMSP F17/F16 satellite cross-track horizontal ion drift along the orbit path at eight intervals between 17 UT on March 13 and 01:30 UT on March 14. The bottom panels in each sub-figure show zoomed-in duskside latitudinal profiles of electron and ion energy flux, ion density, horizontal ion velocity, and vertical ion velocity, respectively. At 17:00 UT (Figure 7a), a noticeable SAPS feature appeared with intense subauroral westward plasma flow between 57 and 62° MLAT equatorward of electron auroral precipitation. SAPS exhibited double-peak structures similar to those mentioned in He et al. (2016) with maximum velocities reaching ∼1,050 m/s at 59.5° and ∼1,100 m/s at 60.5°. These subauroral features were clearly separated from the ion convection returning flow by 6–7° at higher latitudes. A SED signature of local TEC enhancement at 60–65° MLAT can be observed around noon as encircled by a black oval. At 18:45 UT (Figure 7b), both SAPS and SED feature remained prominent. In particular, the SAPS peak shifted

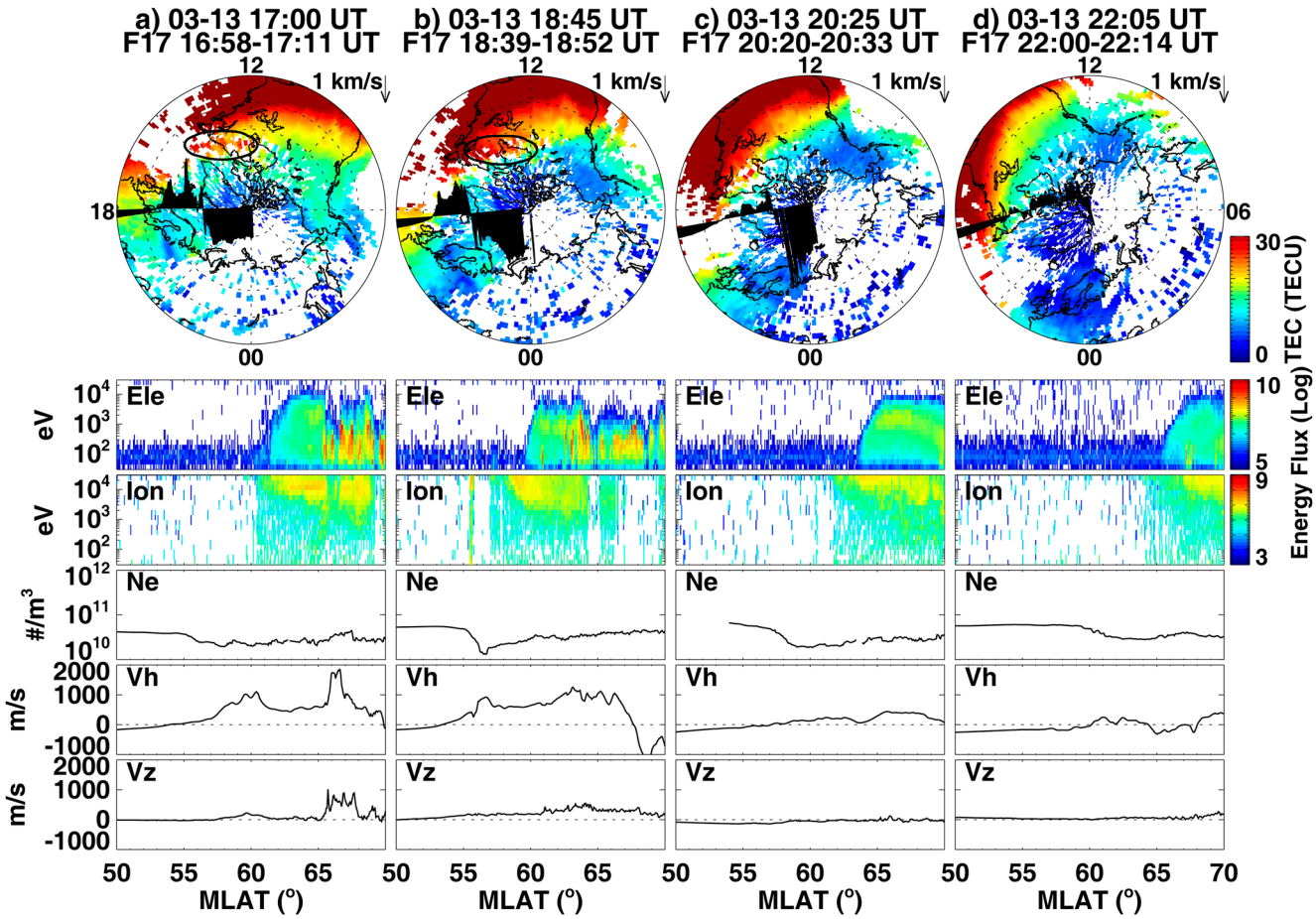

Figure 7. (a–d) Northern Hemisphere polar view of TEC in the magnetic local time and geomagnetic latitude coordinates, overplotted with DMSP F17 satellites horizontal ion velocities at four UT intervals on 13 March 2022. Concentric dashed circles are plotted in 10° intervals with the outermost one representing 40° MLAT. The black oval marks the SED location. The bottom panels in each sub-figure show duskside latitudinal profiles of electron and ion energy flux, ion density, and horizontal and vertical ion drift velocity, respectively.

further equatorward reaching 940 m/s at 56.5° MLAT, collocated with the main trough as shown by the reduced background TEC and electron density depletion in the DMSP profile. The SED plume in this geomagnetic storm was not elongated across the polar cap to form a tongue of ionization (TOI) structure. In comparison, Thomas et al. (2013) presented two distinct SED events with one being evolved into a clear TOI structure and another one being not, under a similar geomagnetic condition with a minimum Sym-H index of −100 nT. Thomas et al. (2013) indicated that the convection electric field played a controlling role in generating a TOI from midlatitude SED.

Nevertheless, SED and SAPS features experienced dramatic temporal variations with suppression and subsequent revival in the following time periods. In particular, SED and SAPS were largely diminished or even disappeared in 2-D GNSS TEC and 1-D profiles at 20:25 UT (Figure 7c) and 22:05 UT (Figure 7d). This is also the time period when IMF Bz was predominantly northward and EIA crests collapsed toward the equator merging into a broad equatorial band (Figures 3b and 3c). However, significant SAPS flows of ∼1,000 m/s reoccurred at 23:20 UT (Figure 8a) and 23:50 UT (Figure 8b) in the dusk sector, manifested in DMSP F16 measurements as an inflection point enhancement of sunward plasma flow at 59° MLAT on the equatorward slope of auroral convection, as well as an independent subauroral westward peak flow at 56° MLAT in DMSP F17 measurements. Such inflection points are common for SAPS latitudinal profiles (Foster & Vo, 2002). Also, SED structures re-appeared at the equatorward edge of SAPS and the main trough. At 00:55 UT (Figure 8c) during storm early recovery phase, a TEC reduction area occurred in the midlatitude afternoon sector, possibly due to the thermospheric composition change effect described earlier. SAPS subsided at this time, though the SED plume was still identifiable and embedded in the nearby density reduction region. At 01:30 UT (Figure 8d), the residue SED plume was

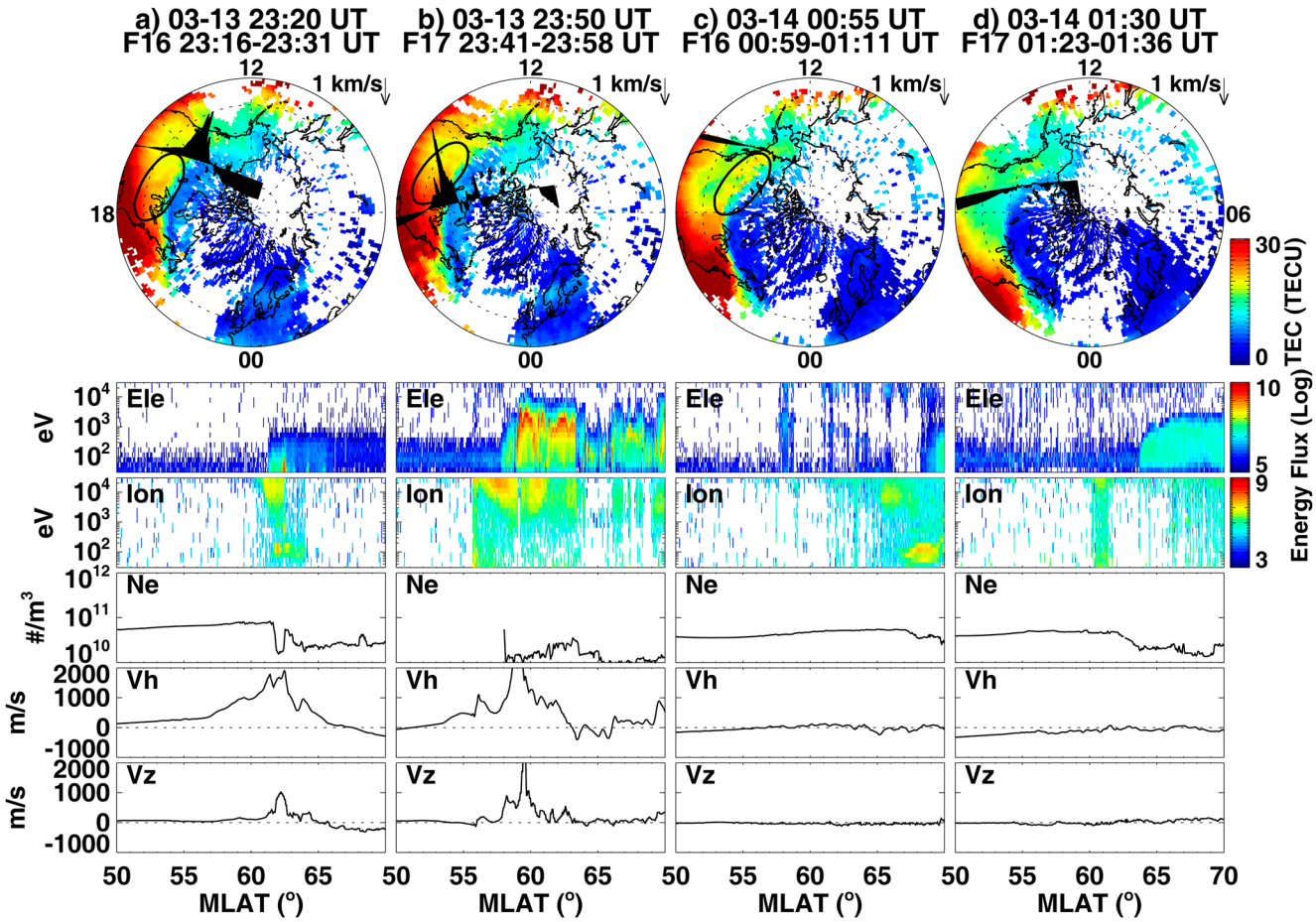

Figure 8. (a–d) The same as Figure 7, but for 23–01 UT on 13–14 March 2022.

completely eroded by the density reduction. Taken as a whole, such a dynamic SED and SAPS variation, with considerable intensification and abatement two times within the storm main phase and early recovery phase, has been rarely reported before and will be further examined in the Discussion section (Section 5).

We next examine the midlatitude thermospheric neutral wind variation using ICON-MIGHTI measurements. Figures 9 and 10 show storm-time and quiet-time ICON-MIGHTI observation tracks and corresponding altitudinal profiles of zonal and meridional wind for six consecutive paths focusing on the American/Atlantic sector between 15 and 24 UT. In Paths 01–03 of Figure 9, the storm-time F-region meridional (zonal) wind had large equatorward (westward) speeds of 50–100 (30–80) m/s in the North American sector, while the quiet-time ones in Figure 10 were much weaker or even with opposite direction, such as the poleward meridional wind. Moreover, the storm-time horizontal winds, especially in Path 02 and 03, showed some hints of wavelike oscillations, representing the existence of strong traveling atmospheric disturbances (TADs) associated with large-scale waves due to storm-time magnetospheric energy deposition in the auroral/subauroral region (Hunsucker, 1982; Zhang et al., 2019). These thermospheric features of large equatorward/westward wind surge associated with large TADs were coincident with the salient ionospheric SED and SAPS during 17–19 UT, and will be discussed together in the next section.

5. Discussion

5.1. Deformation and Reformation of EIA Crests

The dusktime EIA in the American-Atlantic sector exhibited a distinct storm-time deformation and reformation, which merged into a bright equatorial band with almost no density trough during 20:30–22:10 UT on March 13

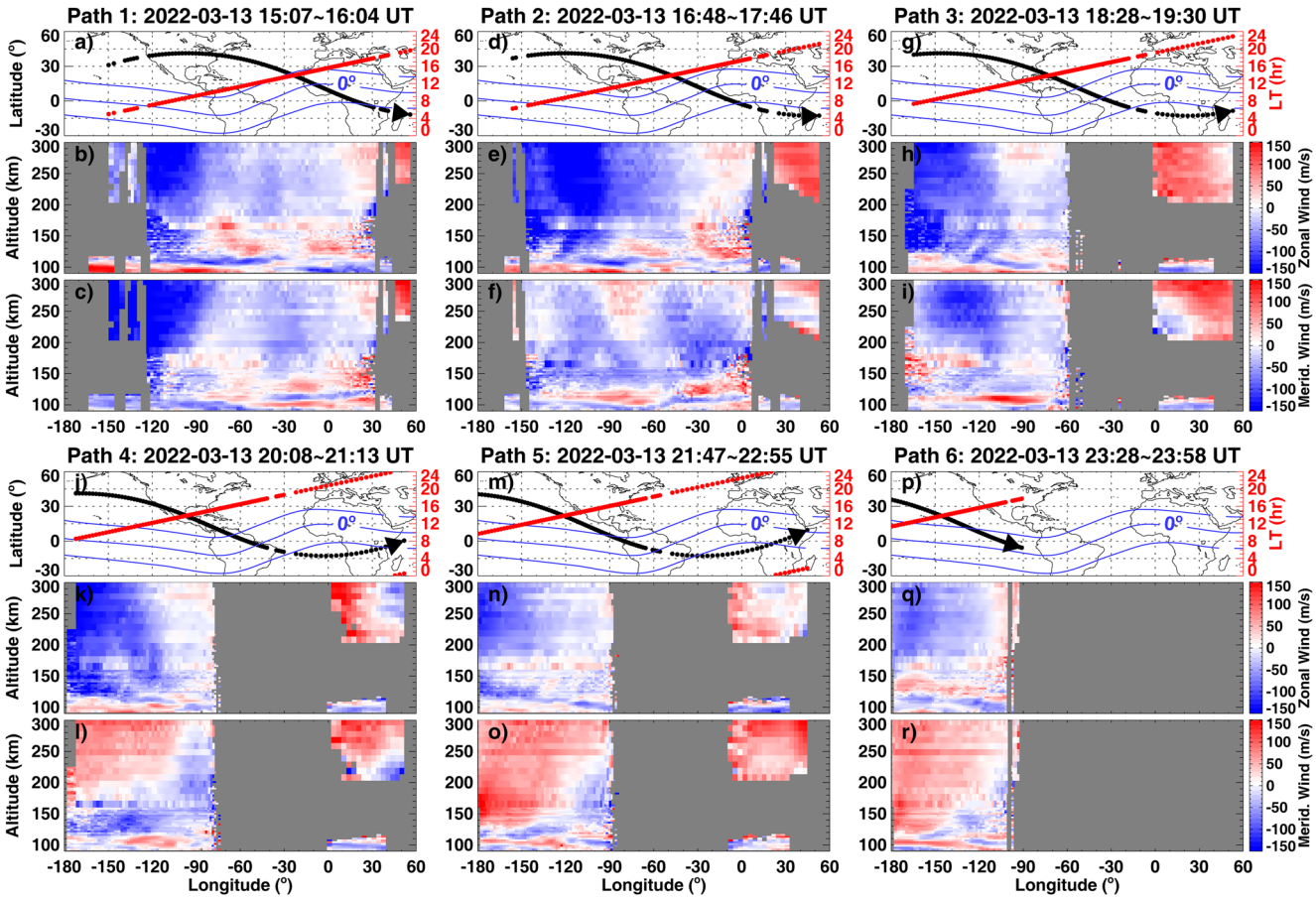

Figure 9. (a–r) ICON MIGHTI observation tracks and corresponding local time, zonal wind (positive eastward), and meridional wind (positive northward) profiles for six consecutive orbits between 15:07–23:58 UT on 13 March 2022. The geomagnetic dip equator and ±15° latitudes are shown by blue lines.

and then quickly separated back into a strong double-peak structure with a broad crest and deep equatorial trough during 23–24 UT. Such a distinct EIA variation could be collectively determined by chemistry and transport due to storm-time E × B drift, ambipolar diffusion, and neutral wind. To further examine such a dynamic EIA variation and discuss the potential impacting factors, Figure 11a shows a TEC keogram as a function of time and latitude along −65° longitude during March 12–14. The mid and low-latitude ionosphere had a positive storm response between 16 and 22 UT on March 13, with 30%–50% absolute TEC enhancement compared with the previous quiet day values. A clear SED signature can be identified around 17–19 UT, which manifested as a poleward-extending plume structure out of the enhanced background TEC in both hemispheres. The quite-time EIA on March 12 showed a typical double-crest structure with two peaks being clearly distinguished. However, storm-time EIA morphology in the crest and trough region on March 13 was completely different. The storm-time EIA crests, especially the northern one, collapsed severely equatorward by ∼10° between 19 and 21 UT, forming a single equatorial band around 21–22 UT, and then quickly separated back into discernible double-crests around 23–24 UT encompassing a deep equatorial trough. This X-pattern EIA merging is similar to that reported in Aa et al. (2022) that mainly attributed to a significant electrodynamic effect of downward plasma drift due to a westward reversal of the equatorial zonal electric field.

To check the potential influence of the electrodynamic effect, Figure 12 shows four ionosonde measurements of electron density (Ne) profile and F2-layer peak height (hmF2) during March 12–15 at Fortaleza, Ramey, Millstone Hill, and Alpena, respectively. As marked by the red arrow in Figure 12a, the hmF2 at the equatorial Fortaleza station showed a noticeable reduction from ∼370 km at 19:50 UT to ∼310 km at 21 UT on March 13 that associated with a considerable peak density (NmF2) enhancement. In comparison, the hmF2 and NmF2 on other days are 40–60 km higher and 20%–30% smaller in the same UT interval, respectively. This indicates that the observed EIA merging was related to the F-layer lowering and suppression of the equatorial fountain due to

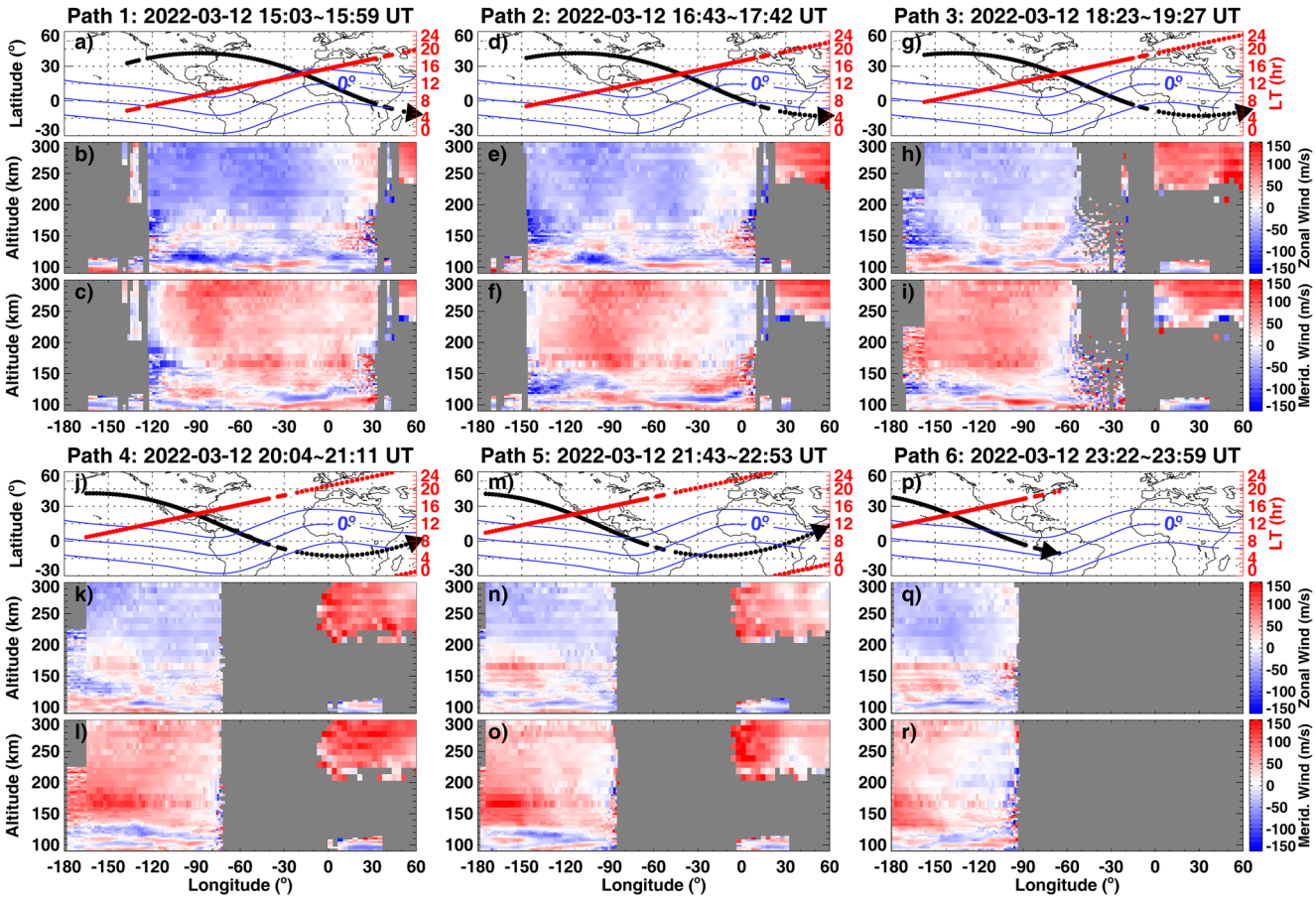

Figure 10. (a–r) The same as Figure 9, but for quiet-time ICON MIGHTI winds measurements on 12 March 2022.

the electrodynamic effect of rapid downward equatorial plasma drift. This was likely caused by the disturbance dynamo and/or possibly an over-shielding penetration electric field with a westward polarity in the daytime, when IMF Bz turned northward and reached a maximum positive value of ∼23 nT at 19:40 UT on March 13. The IMF Bz maintained in the northward direction before reversing back to southward at ∼22 UT.

After the EIA crests merging, Figure 1b shows that IMF Bz drastically reversed to a southward direction with sustained magnitude of below −20 nT between 22:20–23:20 UT. This would create a significant penetration electric field at low latitudes with eastward polarity in the daytime through the dusk, and this overlaid on PRE to considerably increase the equatorial upward E × B drift. As marked by the white arrow in Figure 12a, the equatorial hmF2 at Fortaleza was dramatically lifted to ∼480 km around 24 UT on March 13. This was significantly higher than those of other days where hmF2 was a mere ∼300 km around the same UT. Thus, the EIA double-crest structure quickly reformed with a deep equatorial trough because of an equatorial fountain effect due to the prompt penetration electric field. EIA broadening caused by the electrodynamic effects of penetration electric field during the early storm stages has been extensively reported in other studies (e.g., Lin et al., 2005; Mendillo, 2006; Tsurutani et al., 2008; Zhao et al., 2005).

Besides the consecutive electrodynamic effects from penetration electric fields, could other factors such as composition change or neutral wind play a role in causing such a dynamic EIA merging and separation within 2 hr in the storm main phase? Some studies reported that EIA could be suppressed with a density peak at the equator during storm recovery phase, ascribed to the westward disturbance dynamo electric field and/or the equatorward expansion of neutral composition changes with decreased O/N_2 from higher latitudes (Basu et al., 2009; C. M. Huang et al., 2010; Sreeja et al., 2009). However, it should be noted that this composition change effect of O/N_2 depletion is normally less effective during the early phase of a storm since the ionosphere has already been lifted to high altitudes by the mechanical transport effect of storm-time equatorward neutral wind and/or

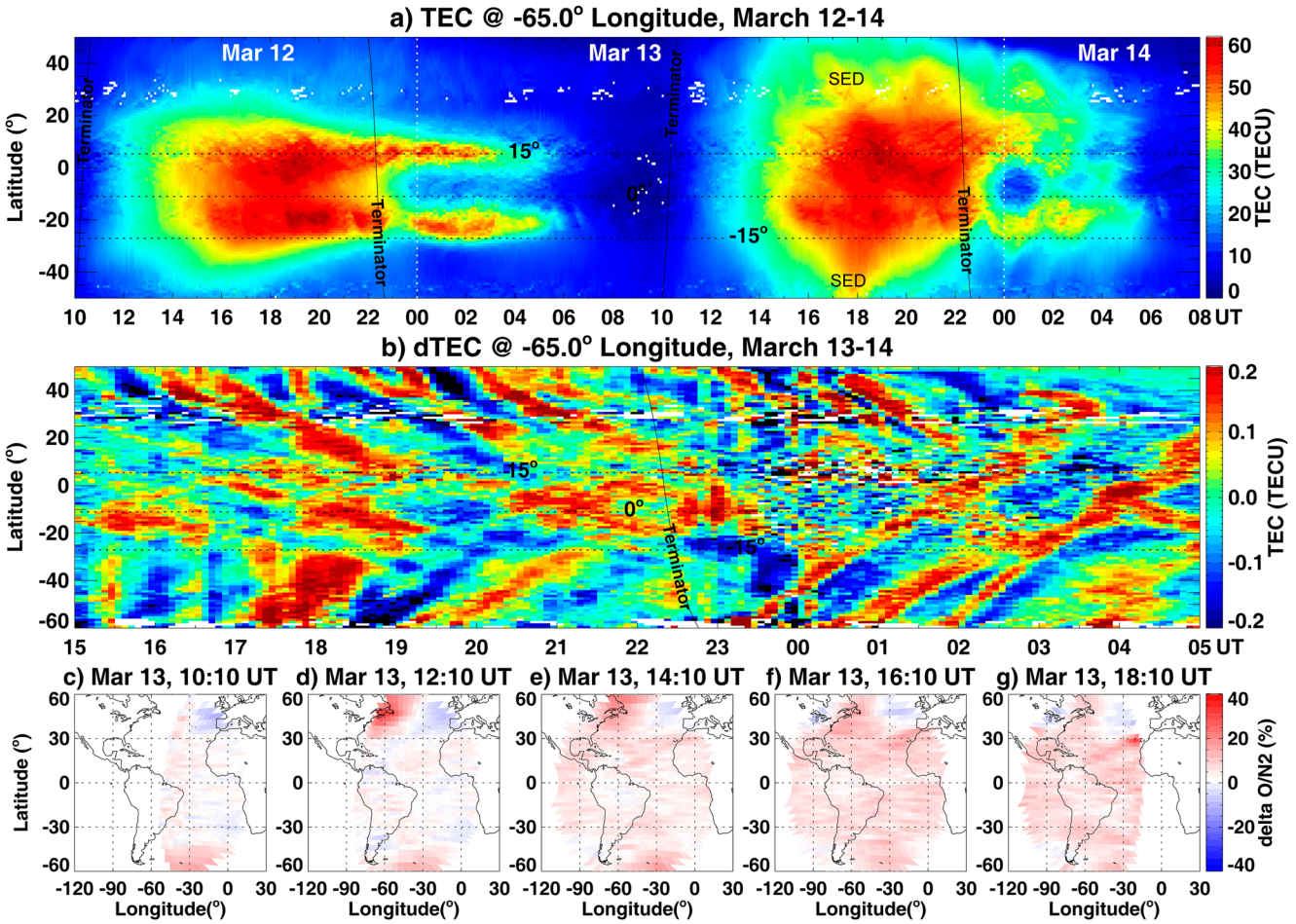

Figure 11. (a) TEC keogram as a function of latitude and UT along −65° longitude and during Mar 12–14, 2022. The terminator and dip equator and ±15° geomagnetic latitudes are also marked. (b) Differential TEC keogram similar to the top panel but for a zoomed period between 15 and 05 UT on Mar 13–14. (c–g) GOLD delta O/N_2 variations between 10:10–18:10 UT on 13 March 2022.

penetration electric field (Balan et al., 2018). In particular, Figures 11c–11g show GOLD delta O/N_2 variations between 10:10 UT–18:10 UT on March 13, computed by subtracting reference values from the previous three and following three quiet-day averages. A majority of the mid- and low-latitude thermosphere experienced increased O/N_2 of 10%–30% during this period, while the decreased O/N_2 was confined to subauroral to high latitudes. Thus, a neutral composition change was unlikely the main driver causing EIA variation under this circumstance.

On the other hand, the disturbance dynamo mechanism might have been built up in the low latitudes during EIA deformation. The disturbance dynamo is primarily caused by the westward neutral wind due to the Coriolis force, which is originally initiated by the equatorward neutral wind generated by Joule heating at auroral latitude (Blanc & Richmond, 1980). ICON-MIGHTI observations in Figure 9 show large equatorward and westward wind surges in the American sector compared with quiet-time measurements (e.g., comparing Figures 9i and 10i). This suggests the existence of the disturbance dynamo. Moreover, the simulation results in Balan et al. (2013) suggest that instead of disturbance dynamo and composition change, the field-aligned plasma convergence from both hemispheres due to the transport of the equatorward neutral wind would be a more effective contribution to equatorial peak dynamics. ICON-MIGHTI results in Figure 9 showed the existence of strong equatorward neutral wind surges and TADs at mid-latitudes, especially in Path 02 and 03 during 17:00–19:30 UT. In Path 04 and 05, the F-region meridional wind around the central American sector was still equatorward although there was a data gap over the Atlantic sector. Therefore, we examined TIDs in this sector using a differential TEC keogram, as shown in Figure 11b, to approximately estimate the potential TAD activity. There were considerable equatorward-propagating TID wavelike features starting from 16 to 17 UT that agree with ICON-MIGHTI results

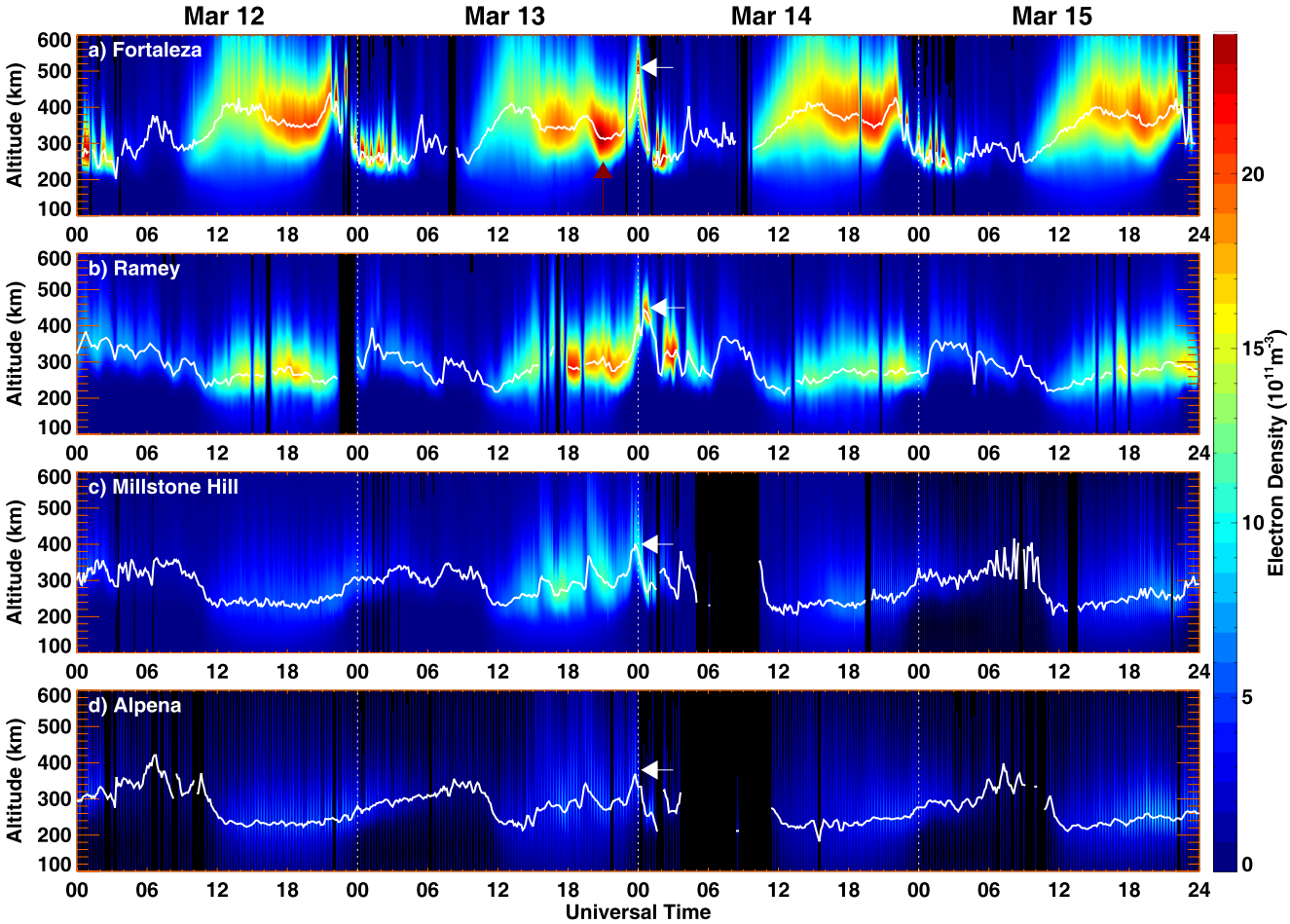

Figure 12. Ionosonde measurements of electron density profiles and F2-layer peak height (hmF2) during 12–15 March 2022 at (a) Fortaleza, (b) Ramey, (c) Millstone Hill, and (d) Alpena, respectively. The white arrows mark a significant storm-time postsunset rise of the equatorial F layer between 23 and 01 UT on March 13–14. The red arrow in panel (a) marks considerable hmF2 decrease and Ne enhancement around 20–21 UT on March 13 at the equatorial Fortaleza station.

in low-latitude regions, which evolved into trans-equatorial TIDs moving toward the other hemisphere during 20–22 UT, around the same time when EIA crests merged into an equatorial band. This suggests that TADs associated with equatorward wind surges due to energy deposition via auroral and Joule heating had likely reached the equatorial area and facilitated plasma convergence as well as disturbance dynamo electric fields therein. The combined transport effect of equatorward neutral wind and electrodynamic effect of disturbance dynamo could collectively play a role to create the observed EIA merging and equatorial peak. A future theoretical study and/or model-data assimilation is needed to further examine neutral wind contributions to these dynamic variations.

5.2. Development of High-Altitude/Latitude EPBs

Strong postsunset EPBs and spread-F irregularities were observed in the American sector after 23:20 UT on March 13, which exhibited field-aligned extensions that cut through EIA crests all the way to the lower mid-latitude area around 30° MLAT. This magnetically maps to an Apex height of ∼2,600 km above the dip equator. Such an abnormally high-latitudinal/altitudinal extension of EPBs has been occasionally reported in the literature. For example, Makela and Kelley (2003) and Shiokawa et al. (2004) reported that high-altitude EPBs in the form of depleted flux tubes can reach 20–25° MLAT at geomagnetic conjugate points, indicating the Apex height reached ∼1,500 km. Mendillo et al. (2005) and Ma and Maruyama (2006) reported that high-altitude EPBs could be observed at lower midlatitude locations above 30° MLAT, similar to the current study. Moreover, some studies found that bubble-like ionospheric depletions could exhibit an extremely large latitudinal extension to mid- and subauroral ionosphere reaching 40° MLAT or even higher latitude (e.g., Aa et al., 2019;

Cherniak & Zakharenkova, 2016; Katamzi-Joseph et al., 2017; Zakharenkova & Cherniak, 2020). Among the above-mentioned studies, the common feature is that all these high-altitude/latitude EPBs were associated with large equatorial upward plasma E × B drift and strong postsunset uplift of the F-layer.

Similarly, in the current event, IMF Bz values rapidly dropped to −20.6 nT at 22:20 UT on March 13 and maintained negative below −20 nT for the next whole hour, suggesting a strong prompt penetration electric field effect with eastward polarity in the dayside through dusk. This is supported by the fact that storm-time hmF2 at all ionosondes in Figure 12 simultaneously showed a much stronger uplift around 23–24 UT on March 13 than on other days, as marked by white arrows. In particular, hmF2 reached a peak value of ∼480 km at the equatorial Fortaleza station and ∼450 km at the low-latitude Ramey station. Such a strong equatorial fountain effect with large upward plasma drift and highly lifted F2 region is a major driver that directly enlarged the Rayleigh-Taylor instability growth rate and pushed EPBs to higher altitudes. Moreover, such a significant postsunset rise of the F-layer could effectively destabilize the elevated bottom-side F-region density gradient with a large instability growth rate due to reduced ion-neutral collision frequency at higher altitudes (Abdu et al., 2009; Sultan, 1996). Thus both Fortaleza and Ramey observed strong spread-F in the ionogram as shown in Figure 6. In addition, these extreme storm-time EPBs developed under a special condition of considerably poleward-moving EIA crests with enhanced background electron densities as previously mentioned. Thus, under these conditions, EPBs would be more favored to reach a higher altitude than usually observed until the flux-tube integrated density depletion match with the enhanced background plasma density with larger scale height (Mendillo et al., 2005; Sousasantos et al., 2023). Taken as a whole, strong penetration electric fields and enhanced background electron density collectively created such abnormal storm-time EPBs with extremely high-altitude/latitude extensions.

5.3. Dynamic Midlatitude SED Characteristics

The midlatitude ionosphere-thermosphere in the American sector experienced significant storm-time disturbances with conspicuous SED and SAPS structures as well as large equatorward (westward) neutral wind surges and strong TAD/TIDs. In particular, the SED signature exhibited a dynamic temporal variation in the storm main phase and early recovery phase, intensifying twice during 17–19 UT and 23–01 UT, respectively. We next briefly discuss the formation mechanism of the SED. (a) Upward E × B drift: These two salient SED signatures appeared shortly after the rapid southward IMF Bz excursion between 16:30–18:00 UT and 22:00–23:30 UT. As previously mentioned, the upward E × B drift due to daytime eastward penetration electric field lifted up the plasma to a higher altitude with a lower recombination rate and corresponding density enhancement (e.g., Heelis et al., 2009; C.-S. Huang et al., 2005; Liu et al., 2016; Zou et al., 2014). The midlatitude ionosonde measurements around the SED region at Millstone Hill (Figure 12c) and Alpena (Figure 12d) show noticeable hmF2 lift-up and electron density enhancement as marked by white arrows due to the above-mentioned electrodynamic effect. (b) Equatorward neutral wind and/or TADs, transporting plasma along the field lines to a higher altitude with lower recombination rates (Balan et al., 2010; Mendillo, 2006). The ICON-MIGHTI neutral wind measurements and GNSS differential TEC results collectively showed the presence of equatorward neutral wind surge and TID/TADs. (c) Zonal flux transport driven by SAPS: As shown in Figures 7 and 8, the intensification and decay of SED were simultaneously associated with the alternate presence and absence of distinct SAPS flows along the plume's poleward edge. This implies that plume materials could be carried from the nightside to the dayside in the SAPS overlapping region as seen in other SED/SAPS studies (Foster et al., 2007). This strong sunward flow is against the rotational electric field direction, and therefore could cause the temporary stagnation of plasma flow on the dayside with respect to the ground. (d) Thermospheric composition change effect: The downwelling of neutral species through constant pressure levels, providing atomic oxygen-rich air at mid- and low-latitudes, could enhance the column electron density, facilitating TEC/Ne enhancements within SED (Immel et al., 2001; W. Wang et al., 2012). This can be deduced from Figures 11c–11g with large dayside O/N_2 enhancement at mid and low-latitudes (but not limited to the SED region). In conclusion, the dynamic temporal variation of the SED plume, which intensified and diminished twice, was closely preceded by and correlated with southward IMF Bz. This indicates the controlling role of high-latitude convection and penetration electric fields in generating SED in this event, consistent with that demonstrated in Thomas et al. (2013). A future modeling study is needed to quantify the contribution of other processes.

6. Conclusions

In this study, we have investigated the mid- and low-latitude ionosphere responses over the American/Atlantic sector during a moderate but effective geomagnetic storm on 13–14 March 2022, utilizing multi-instrument data

from ground-based GNSS TEC and ionosondes observations, as well as space-borne measurements from GOLD, ICON, Swarm, and DMSP satellites. A series of salient storm-induced ionospheric disturbances and associated electrodynamics and neutral dynamics were analyzed and summarized as follows.

1. The low-latitude EIA morphology exhibited a distinct storm-time deformation and reformation, which merged into a bright equatorial band with almost no trough during 20:30–22:10 UT on March 13 and then quickly separated back into a strong double-peak structure with a large crest width and a deep equatorial density trough during 23–24 UT. The EIA merging could be collectively caused by the plasma convergence due to the mechanical effect of equatorward-propagating neutral wind and TADs, by the electrodynamic effect with downward equatorial plasma drift due to the disturbance dynamo and/or by an over-shielding electric field. The EIA reformation and broadening were caused by the enhanced fountain effect due to the prompt penetration electric field.
2. Strong postsunset EPBs and spread-F irregularities were observed since 23:20 UT on March 13 and continued for a few hours, with an abnormally high-latitudinal extension that cut through EIA crests all the way to the lower midlatitude area around 30° MLAT. This indicates EPBs can rise to an Apex height of ∼2,600 km above the dip equator. Such an extremely high-altitude/latitude EPB event was likely caused by a significant equatorial postsunset rise of the F-layer due to a strong eastward penetration electric field near local dusk, under a favorable condition of broadened EIA crests with enhanced background density.
3. The midlatitude ionosphere experienced a conspicuous SED structure that exhibited an unusual temporal variation associated with SAPS. This feature intensified and diminished twice during 17–19 UT and 23–01 UT on March 13–14, respectively. Such a dynamic SED variation could be mainly attributed to electrodynamic effects due to the repeated polarity reversal of penetration electric field, plus contributions from the composition change effect and equatorward neutral wind surge.

The uniqueness of this storm event is the simultaneous occurrence of these three characteristic low and mid-latitude ionospheric disturbances that are predominantly driven by a key factor of strong penetration electric fields. This indicates that even a moderate storm can be significantly geo-effective in generating substantial electrodynamic processes throughout the global ionosphere with considerable impacts on both plasma and neutral dynamics.

Data Availability Statement

GNSS TEC data products are provided through the Madrigal distributed data system at (http://cedar.openmadrigal.org/) by MIT Haystack Observatory. The GOLD data can be accessed at (https://gold.cs.ucf.edu/data/). The ICON data can be accessed at (https://icon.ssl.berkeley.edu/Data). The solar wind and geophysical parameters data are acquired from NASA/GSFC's Space Physics Data Facility's OMNIWeb service (https://cdaweb.gsfc.nasa.gov/) and Kyoto world data center for Geomagnetism (http://wdc.kugi.kyoto-u.ac.jp/). The ionosonde data are provided by the University of Massachusetts Lowell DIDB database of Global Ionospheric Radio Observatory (https://giro.uml.edu/didbase/scaled.php). The DMSP SSIES and SSJ data are available at NOAA NGDC (satdat.ngdc.noaa.gov/dmsp/) and the Madrigal CEDAR database (http://cedar.openmadrigal.org/). Swarm data are provided by European Space Agency (https://swarmdiss.eo.esa.int/).

Acknowledgments
GNSS TEC data are generated as part of the Millstone Hill Geospace Facility program, operated by the Massachusetts Institute of Technology under NSF AGS-1952737. We acknowledge NSF awards AGS-2033787, AGS-2033843, AGS-2149698, PHY-2028125, and NSFC41974184, NASA support 80NSSC22K0171, 80NSSC21K1310, 80NSSC21K1775, 80NSSC19K0834, 80NSSC19K0078, 80NSSC17K0013, 80NSSC19K0835, 80NSSC20K0601, 80NSSC20K0356, 80NSSC20K1785, and 80GSFC22CA011, AFOSR MURI Project FA9559-16-1-0364, and ONR Grant N00014-17-1-2186 and N00014-22-1-2284. Data for TEC processing is provided from the following organizations: UNAVCO, SOPAC, IGN (France), IGS, CDDIS, NGS, IBGE (Brazil), RAMSAC (Argentina), CORS (Panama), Arecibo Observatory, LISN, Topcon, CHAIN (Canada), CRS (Italy), SONEL, RENAG (New Zealand), GNSS Reference Networks, Finnish Meteorological Institute, and SWEPOS. National Center for Atmospheric Research is sponsored by the National Science Foundation.

References

Aa, E., Huang, W., Liu, S., Ridley, A., Zou, S., Shi, L., et al. (2018). Midlatitude plasma bubbles over China and adjacent areas during a magnetic storm on 8 September 2017. *Space Weather*, *16*(3), 321–331. https://doi.org/10.1002/2017SW001776

Aa, E., Zhang, S.-R., Erickson, P. J., Coster, A. J., Goncharenko, L. P., Varney, R. H., & Eastes, R. (2021). Salient midlatitude ionosphere-thermosphere disturbances associated with SAPS during a minor but geo-effective storm at deep solar minimum. *Journal of Geophysical Research: Space Physics*, *126*(7), e29509. https://doi.org/10.1029/2021JA029509

Aa, E., Zhang, S.-R., Liu, G., Eastes, R. W., Wang, W., Karan, D. K., et al. (2023). Statistical analysis of equatorial plasma bubbles climatology and multi-day periodicity using GOLD observations. *Geophysical Research Letters*, *50*(8), e2023GL103510. https://doi.org/10.1029/2023GL103510

Aa, E., Zhang, S.-R., Wang, W., Erickson, P. J., Qian, L., Eastes, R., et al. (2022). Pronounced suppression and X-pattern merging of equatorial ionization anomalies after the 2022 Tonga Volcano eruption. *Journal of Geophysical Research: Space Physics*, *127*(6), e30527. https://doi.org/10.1029/2022JA030527

Aa, E., Zou, S., Eastes, R., Karan, D. K., Zhang, S.-R., Erickson, P. J., & Coster, A. J. (2020). Coordinated ground-based and space-based observations of equatorial plasma bubbles. *Journal of Geophysical Research: Space Physics*, *125*(1), e27569. https://doi.org/10.1029/2019JA027569

Aa, E., Zou, S., Ridley, A., Zhang, S., Coster, A. J., Erickson, P. J., et al. (2019). Merging of storm time midlatitude traveling ionospheric disturbances and equatorial plasma bubbles. *Space Weather*, *17*(2), 285–298. https://doi.org/10.1029/2018SW002101

Abdu, M. A. (2019). Day-to-day and short-term variabilities in the equatorial plasma bubble/spread F irregularity seeding and development. *Progress in Earth and Planetary Science*, *6*(1), 11. https://doi.org/10.1186/s40645-019-0258-1

Abdu, M. A. (2001). Outstanding problems in the equatorial ionosphere-thermosphere electrodynamics relevant to spread F. *Journal of Atmospheric and Solar-Terrestrial Physics*, *63*(9), 869–884. https://doi.org/10.1016/S1364-6826(00)00201-7

Abdu, M. A., Alam Kherani, E., Batista, I. S., de Paula, E. R., Fritts, D. C., & Sobral, J. H. A. (2009). Gravity wave initiation of equatorial spread F/plasma bubble irregularities based on observational data from the SpreadFEx campaign. *Annales Geophysicae*, *27*(7), 2607–2622. https://doi.org/10.5194/angeo-27-2607-2009

Abdu, M. A., de Medeiros, R. T., & Sobral, J. H. A. (1982). Equatorial spread F instability conditions as determined from ionograms. *Geophysical Research Letters*, *9*(6), 692–695. https://doi.org/10.1029/GL009i006p00692

Anderson, D. N. (1976). Modeling the midlatitude F-region ionospheric storm using east-west drift and a meridional wind. *Planetary and Space Science*, *24*(1), 69–77. https://doi.org/10.1016/0032-0633(76)90063-5

Appleton, E. V. (1946). Two anomalies in the ionosphere. *Nature*, *157*(3995), 691. https://doi.org/10.1038/157691a0

Astafyeva, E., Yasyukevich, Y. V., Maletckii, B., Oinats, A., Vesnin, A., Yasyukevich, A. S., et al. (2022). Ionospheric disturbances and irregularities during the 25-26 August 2018 geomagnetic storm. *Journal of Geophysical Research: Space Physics*, *127*(1), e29843. https://doi.org/10.1029/2021JA029843

Astafyeva, E., Zakharenkova, I., Hozumi, K., Alken, P., Coïsson, P., Hairston, M. R., & Coley, W. R. (2018). Study of the equatorial and low-latitude electrodynamic and ionospheric disturbances during the 22-23 June 2015 geomagnetic storm using ground-based and spaceborne techniques. *Journal of Geophysical Research: Space Physics*, *123*(3), 2424–2440. https://doi.org/10.1002/2017JA024981

Balan, N., Liu, L., & Le, H. (2018). A brief review of equatorial ionization anomaly and ionospheric irregularities. *Earth and Planetary Physics*, *2*(4), 257–275. https://doi.org/10.26464/epp2018025

Balan, N., Otsuka, Y., Nishioka, M., Liu, J. Y., & Bailey, G. J. (2013). Physical mechanisms of the ionospheric storms at equatorial and higher latitudes during the recovery phase of geomagnetic storms. *Journal of Geophysical Research: Space Physics*, *118*(5), 2660–2669. https://doi.org/10.1002/jgra.50275

Balan, N., Shiokawa, K., Otsuka, Y., Kikuchi, T., Vijaya Lekshmi, D., Kawamura, S., et al. (2010). A physical mechanism of positive ionospheric storms at low latitudes and midlatitudes. *Journal of Geophysical Research*, *115*(A2), A02304. https://doi.org/10.1029/2009JA014515

Balan, N., Shiokawa, K., Otsuka, Y., Watanabe, S., & Bailey, G. J. (2009). Super plasma fountain and equatorial ionization anomaly during penetration electric field. *Journal of Geophysical Research*, *114*(A3), A03310. https://doi.org/10.1029/2008JA013768

Basu, S., Basu, S., Huba, J., Krall, J., McDonald, S. E., Makela, J. J., et al. (2009). Day-to-day variability of the equatorial ionization anomaly and scintillations at dusk observed by GUVI and modeling by SAMI3. *Journal of Geophysical Research*, *114*(A4), A04302. https://doi.org/10.1029/2008JA013899

Basu, S., Basu, S., Rich, F. J., Groves, K. M., MacKenzie, E., Coker, C., et al. (2007). Response of the equatorial ionosphere at dusk to penetration electric fields during intense magnetic storms. *Journal of Geophysical Research*, *112*(A8), A08308. https://doi.org/10.1029/2006JA012192

Blanc, M., & Richmond, A. D. (1980). The ionospheric disturbance dynamo. *Journal of Geophysical Research*, *85*(A4), 1669–1686. https://doi.org/10.1029/JA085iA04p01669

Buonsanto, M. J. (1999). Ionospheric storms — A review. *Space Science Reviews*, *88*(3/4), 563–601. https://doi.org/10.1023/A:1005107532631

Cai, X., Burns, A. G., Wang, W., Qian, L., Liu, J., Solomon, S. C., et al. (2021). Observation of postsunset OI 135.6 nm radiance enhancement over South America by the GOLD mission. *Journal of Geophysical Research: Space Physics*, *126*(2), e28108. https://doi.org/10.1029/2020JA028108

Cai, X., Burns, A. G., Wang, W., Qian, L., Pedatella, N., Coster, A., et al. (2021). Variations in thermosphere composition and ionosphere total electron content under "Geomagnetically Quiet" conditions at solar-minimum. *Geophysical Research Letters*, *48*(11), e93300. https://doi.org/10.1029/2021GL093300

Cai, X., Burns, A. G., Wang, W., Qian, L., Solomon, S. C., Eastes, R. W., et al. (2020). The two-dimensional evolution of thermospheric $\sum O/N_2$ response to weak geomagnetic activity during solar-minimum observed by GOLD. *Geophysical Research Letters*, *47*(18), e88838. https://doi.org/10.1029/2020GL088838

Cai, X., Qian, L., Wang, W., McInerney, J. M., Liu, H.-L., & Eastes, R. W. (2022). Investigation of the post-sunset extra electron density peak poleward of the equatorial ionization anomaly southern crest. *Journal of Geophysical Research: Space Physics*, *127*(9). e2022JA030755. https://doi.org/10.1029/2022JA030755

Cai, X., Wang, W., Eastes, R. W., Qian, L., Pedatella, N. M., Aa, E., et al. (2023). Equatorial ionization anomaly discontinuity observed by GOLD, COSMIC-2, and ground-based GPS receivers' network. *Geophysical Research Letters*, *50*(10), e2023GL102994. https://doi.org/10.1029/2023GL102994

Carter, B. A., Yizengaw, E., Pradipta, R., Retterer, J. M., Groves, K., Valladares, C., et al. (2016). Global equatorial plasma bubble occurrence during the 2015 St. Patrick's Day storm. *Journal of Geophysical Research: Space Physics*, *121*(1), 894–905. https://doi.org/10.1002/2015JA022194

Chang, H., Kil, H., Sun, A. K., Zhang, S.-R., & Lee, J. (2022). Ionospheric disturbances in low- and midlatitudes during the geomagnetic storm on 26 August 2018. *Journal of Geophysical Research: Space Physics*, *127*(2), e2021JA029879. https://doi.org/10.1029/2021JA029879

Cherniak, I., & Zakharenkova, I. (2016). First observations of super plasma bubbles in Europe. *Geophysical Research Letters*, *43*(21), 11137–11145. https://doi.org/10.1002/2016GL071421

Cherniak, I., & Zakharenkova, I. (2022). Development of the storm-induced ionospheric irregularities at equatorial and middle latitudes during the 25-26 August 2018 geomagnetic storm. *Space Weather*, *20*(2), e2021SW002891. https://doi.org/10.1029/2021SW002891

Coster, A. J., Colerico, M. J., Foster, J. C., Rideout, W., & Rich, F. (2007). Longitude sector comparisons of storm enhanced density. *Geophysical Research Letters*, *34*(18), L18105. https://doi.org/10.1029/2007GL030682

Datta-Barua, S., Bust, G. S., & Crowley, G. (2011). Deducing storm time F region ionospheric dynamics from 3-D time-varying imaging. *Journal of Geophysical Research*, *116*(A5), A05324. https://doi.org/10.1029/2010JA016304

David, M., Sojka, J. J., Schunk, R. W., Liemohn, M. W., & Coster, A. J. (2011). Dayside midlatitude ionospheric response to storm time electric fields: A case study for 7 September 2002. *Journal of Geophysical Research*, *116*(A12), A12302. https://doi.org/10.1029/2011JA016988

Deng, Y., & Ridley, A. J. (2006). Role of vertical ion convection in the high-latitude ionospheric plasma distribution. *Journal of Geophysical Research*, *111*(A9), A09314. https://doi.org/10.1029/2006JA011637

Duncan, R. A. (1960). The equatorial F-region of the ionosphere. *Journal of Atmospheric and Terrestrial Physics*, *18*(2), 89–100. https://doi.org/10.1016/0021-9169(60)90081-7

Eastes, R. W., McClintock, W. E., Burns, A. G., Anderson, D. N., Andersson, L., Aryal, S., et al. (2020). Initial observations by the GOLD mission. *Journal of Geophysical Research: Space Physics*, *125*(7), e27823. https://doi.org/10.1029/2020JA027823

Eastes, R. W., McClintock, W. E., Burns, A. G., Anderson, D. N., Andersson, L., Codrescu, M., et al. (2017). The Global-Scale Observations of the Limb and Disk (GOLD) mission. *Space Science Reviews*, *212*(1–2), 383–408. https://doi.org/10.1007/s11214-017-0392-2

Eastes, R. W., Solomon, S. C., Daniell, R. E., Anderson, D. N., Burns, A. G., England, S. L., et al. (2019). Global-scale observations of the equatorial ionization anomaly. *Geophysical Research Letters*, *46*(16), 9318–9326. https://doi.org/10.1029/2019GL084199

Fejer, B. G. (2002). Low latitude storm time ionospheric electrodynamics. *Journal of Atmospheric and Solar-Terrestrial Physics*, *64*(12–14), 1401–1408. https://doi.org/10.1016/S1364-6826(02)00103-7

Fejer, B. G., Scherliess, L., & de Paula, E. R. (1999). Effects of the vertical plasma drift velocity on the generation and evolution of equatorial spread F. *Journal of Geophysical Research*, *104*(A9), 19859–19870. https://doi.org/10.1029/1999JA900271

Ferdousi, B., Nishimura, Y., Maruyama, N., & Lyons, L. R. (2019). Subauroral neutral wind driving and its feedback to SAPS during the 17 March 2013 geomagnetic storm. *Journal of Geophysical Research: Space Physics*, *124*(3), 2323–2337. https://doi.org/10.1029/2018JA026193

Foster, J. C. (1993). Storm time plasma transport at middle and high latitudes. *Journal of Geophysical Research*, *98*(A2), 1675–1690. https://doi.org/10.1029/92JA02032

Foster, J. C., & Burke, W. J. (2002). SAPS: A new categorization for sub-auroral electric fields. *EOS Transactions*, *83*(36), 393. https://doi.org/10.1029/2002EO000289

Foster, J. C., & Coster, A. J. (2007). Conjugate localized enhancement of total electron content at low latitudes in the American sector. *Journal of Atmospheric and Solar-Terrestrial Physics*, *69*(10–11), 1241–1252. https://doi.org/10.1016/j.jastp.2006.09.012

Foster, J. C., & Rideout, W. (2005). Midlatitude TEC enhancements during the October 2003 superstorm. *Geophysical Research Letters*, *32*(12), L12S04. https://doi.org/10.1029/2004GL021719

Foster, J. C., Rideout, W., Sandel, B., Forrester, W. T., & Rich, F. J. (2007). On the relationship of SAPS to storm-enhanced density. *Journal of Atmospheric and Solar-Terrestrial Physics*, *69*(3), 303–313. https://doi.org/10.1016/j.jastp.2006.07.021

Foster, J. C., & Vo, H. B. (2002). Average characteristics and activity dependence of the subauroral polarization stream. *Journal of Geophysical Research*, *107*(A12), SIA16-1–SIA16-10. https://doi.org/10.1029/2002JA009409

Foster, J. C., Zou, S., Heelis, R. A., & Erickson, P. J. (2021). Ionospheric storm-enhanced density plumes. In *Ionosphere dynamics and applications* (pp. 115–126). American Geophysical Union (AGU). https://doi.org/10.1002/9781119815617.ch6

Friis-Christensen, E., Lühr, H., Knudsen, D., & Haagmans, R. (2008). Swarm-An Earth observation mission investigating geospace. *Advances in Space Research*, *41*(1), 210–216. https://doi.org/10.1016/j.asr.2006.10.008

Fuller-Rowell, T. J., Codrescu, M. V., Moffett, R. J., & Quegan, S. (1994). Response of the thermosphere and ionosphere to geomagnetic storms. *Journal of Geophysical Research*, *99*(A3), 3893–3914. https://doi.org/10.1029/93JA02015

Fuller-Rowell, T. J., Millward, G. H., Richmond, A. D., & Codrescu, M. V. (2002). Storm-time changes in the upper atmosphere at low latitudes. *Journal of Atmospheric and Solar-Terrestrial Physics*, *64*(12–14), 1383–1391. https://doi.org/10.1016/S1364-6826(02)00101-3

Gardner, L. C., Schunk, R. W., Scherliess, L., Eccles, V., Basu, S., & Valladeres, C. (2018). Modeling the midlatitude ionosphere storm-enhanced density distribution with a data assimilation model. *Space Weather*, *16*(10), 1539–1548. https://doi.org/10.1029/2018SW001882

Harding, B. J., Makela, J. J., Englert, C. R., Marr, K. D., Harlander, J. M., England, S. L., & Immel, T. J. (2017). The MIGHTI wind retrieval algorithm: Description and verification. *Space Science Reviews*, *212*(1–2), 585–600. https://doi.org/10.1007/s11214-017-0359-3

He, F., Zhang, X.-X., Wang, W., & Chen, B. (2016). Double-peak subauroral ion drifts (DSAIDs). *Geophysical Research Letters*, *43*(11), 5554–5562. https://doi.org/10.1002/2016GL069133

Heelis, R. A. (2004). Electrodynamics in the low and middle latitude ionosphere: A tutorial. *Journal of Atmospheric and Solar-Terrestrial Physics*, *66*(10), 825–838. https://doi.org/10.1016/j.jastp.2004.01.034

Heelis, R. A., Sojka, J. J., David, M., & Schunk, R. W. (2009). Storm time density enhancements in the middle-latitude dayside ionosphere. *Journal of Geophysical Research*, *114*(A3), A03315. https://doi.org/10.1029/2008JA013690

Huang, C. M., Chen, M. Q., & Liu, J. Y. (2010). Ionospheric positive storm phases at the magnetic equator close to sunset. *Journal of Geophysical Research*, *115*(A7), A07315. https://doi.org/10.1029/2009JA014936

Huang, C.-S., Foster, J. C., Goncharenko, L. P., Erickson, P. J., Rideout, W., & Coster, A. J. (2005). A strong positive phase of ionospheric storms observed by the Millstone Hill incoherent scatter radar and global GPS network. *Journal of Geophysical Research*, *110*(A6), A06303. https://doi.org/10.1029/2004JA010865

Huang, C.-S., Sazykin, S., Chau, J. L., Maruyama, N., & Kelley, M. C. (2007). Penetration electric fields: Efficiency and characteristic time scale. *Journal of Atmospheric and Solar-Terrestrial Physics*, *69*(10–11), 1135–1146. https://doi.org/10.1016/j.jastp.2006.08.016

Huba, J. D., Sazykin, S., & Coster, A. (2017). SAMI3-RCM simulation of the 17 March 2015 geomagnetic storm. *Journal of Geophysical Research: Space Physics*, *122*(1), 1246–1257. https://doi.org/10.1002/2016JA023341

Hunsucker, R. D. (1982). Atmospheric gravity waves generated in the high-latitude ionosphere: A review (Paper 1R1822). *Reviews of Geophysics and Space Physics*, *20*(2), 293. https://doi.org/10.1029/RG020i002p00293

Immel, T. J., Crowley, G., Craven, J. D., & Roble, R. G. (2001). Dayside enhancements of thermospheric O/N_2 following magnetic storm onset. *Journal of Geophysical Research*, *106*(A8), 15471–15488. https://doi.org/10.1029/2000JA000096

Immel, T. J., England, S. L., Mende, S. B., Heelis, R. A., Englert, C. R., Edelstein, J., et al. (2018). The ionospheric connection explorer mission: Mission goals and design. *Space Science Reviews*, *214*(1), 13. https://doi.org/10.1007/s11214-017-0449-2

Katamzi-Joseph, Z. T., Habarulema, J. B., & Hernández-Pajares, M. (2017). Midlatitude postsunset plasma bubbles observed over Europe during intense storms in April 2000 and 2001. *Space Weather*, *15*(9), 1177–1190. https://doi.org/10.1002/2017SW001674

Kelley, M. C., Haerendel, G., Kappler, H., Valenzuela, A., Balsley, B. B., Carter, D. A., et al. (1976). Evidence for a Rayleigh-Taylor type instability and upwelling of depleted density regions during equatorial spread F. *Geophysical Research Letters*, *3*(8), 448–450. https://doi.org/10.1029/GL003i008p00448

Kikuchi, T., Araki, T., Maeda, H., & Maekawa, K. (1978). Transmission of polar electric fields to the equator. *Nature*, *273*(5664), 650–651. https://doi.org/10.1038/273650a0

Kil, H., Paxton, L. J., Su, S.-Y., Zhang, Y., & Yeh, H. (2006). Characteristics of the storm-induced big bubbles (SIBBs). *Journal of Geophysical Research*, *111*(A10), A10308. https://doi.org/10.1029/2006JA011743

Li, G., Ning, B., Liu, L., Wan, W., & Liu, J. Y. (2009). Effect of magnetic activity on plasma bubbles over equatorial and low-latitude regions in East Asia. *Annales Geophysicae*, *27*(1), 303–312. https://doi.org/10.5194/angeo-27-303-2009

Lin, C. H., Richmond, A. D., Liu, J. Y., Yeh, H. C., Paxton, L. J., Lu, G., et al. (2005). Large-scale variations of the low-latitude ionosphere during the October-November 2003 superstorm: Observational results. *Journal of Geophysical Research*, *110*(A9), A09S28. https://doi.org/10.1029/2004JA010900

Liu, J., Wang, W., Burns, A., Solomon, S. C., Zhang, S., Zhang, Y., & Huang, C. (2016). Relative importance of horizontal and vertical transports to the formation of ionospheric storm-enhanced density and polar tongue of ionization. *Journal of Geophysical Research: Space Physics*, *121*(8), 8121–8133. https://doi.org/10.1002/2016JA022882

Lu, G., Goncharenko, L. P., Richmond, A. D., Roble, R. G., & Aponte, N. (2008). A dayside ionospheric positive storm phase driven by neutral winds. *Journal of Geophysical Research*, *113*(A8), A08304. https://doi.org/10.1029/2007JA012895

Luan, X. (2021). Equatorial ionization anomaly variations during geomagnetic storms. In *Ionosphere dynamics and applications* (pp. 301–312). American Geophysical Union (AGU). https://doi.org/10.1002/9781119815617.ch13

Ma, G., & Maruyama, T. (2006). A super bubble detected by dense GPS network at East Asian longitudes. *Geophysical Research Letters*, *33*(21), L21103. https://doi.org/10.1029/2006GL027512

Makela, J. J., & Kelley, M. C. (2003). Field-aligned 777.4-nm composite airglow images of equatorial plasma depletions. *Geophysical Research Letters*, *30*(8), 1442. https://doi.org/10.1029/2003GL017106

Mannucci, A. J., Tsurutani, B. T., Iijima, B. A., Komjathy, A., Saito, A., Gonzalez, W. D., et al. (2005). Dayside global ionospheric response to the major interplanetary events of October 29-30, 2003 "Halloween Storms". *Geophysical Research Letters*, *32*(12), L12S02. https://doi.org/10.1029/2004GL021467

Maruyama, N., Richmond, A. D., Fuller-Rowell, T. J., Codrescu, M. V., Sazykin, S., Toffoletto, F. R., et al. (2005). Interaction between direct penetration and disturbance dynamo electric fields in the storm-time equatorial ionosphere. *Geophysical Research Letters*, *32*(17), L17105. https://doi.org/10.1029/2005GL023763

Mendillo, M. (2006). Storms in the ionosphere: Patterns and processes for total electron content. *Reviews of Geophysics*, *44*(4), RG4001. https://doi.org/10.1029/2005RG000193

Mendillo, M., Zesta, E., Shodhan, S., Sultan, P. J., Doe, R., Sahai, Y., & Baumgardner, J. (2005). Observations and modeling of the coupled latitude-altitude patterns of equatorial plasma depletions. *Journal of Geophysical Research*, *110*(A9), A09303. https://doi.org/10.1029/2005JA011157

Moldwin, M. B., Zou, S., & Heine, T. (2016). The story of plumes: The development of a new conceptual framework for understanding magnetosphere and ionosphere coupling. *Annales Geophysicae*, *34*(12), 1243–1253. https://doi.org/10.5194/angeo-34-1243-2016

Mrak, S., Semeter, J., Nishimura, Y., Rodrigues, F. S., Coster, A. J., & Groves, K. (2020). Leveraging geodetic GPS receivers for ionospheric scintillation science. *Radio Science*, *55*(11), e2020RS007131. https://doi.org/10.1029/2020RS007131

Nava, B., Rodríguez-Zuluaga, J., Alazo-Cuartas, K., Kashcheyev, A., Migoya-Orué, Y., Radicella, S. M., et al. (2016). Middle- and low-latitude ionosphere response to 2015 St. Patrick's Day geomagnetic storm. *Journal of Geophysical Research: Space Physics*, *121*(4), 3421–3438. https://doi.org/10.1002/2015JA022299

Nishimura, Y., Mrak, S., Semeter, J. L., Coster, A. J., Jayachandran, P. T., Groves, K. M., et al. (2021). Evolution of mid-latitude density irregularities and scintillation in North America during the 7-8 September 2017 storm. *Journal of Geophysical Research: Space Physics*, *126*(6), e29192. https://doi.org/10.1029/2021JA029192

Prölss, G. W. (1980). Magnetic storm associated perturbations of the upper atmosphere - Recent results obtained by satellite-borne gas analyzers. *Reviews of Geophysics and Space Physics*, *18*(1), 183–202. https://doi.org/10.1029/RG018i001p00183

Prölss, G. W. (2008). *Ionospheric storms at mid-latitude: A short review* (Vol. 181, pp. 9–24). American Geophysical Union Geophysical Monograph Series. https://doi.org/10.1029/181GM03

Prölss, G. W. (2011). Density perturbations in the upper atmosphere caused by the dissipation of solar wind energy. *Surveys in Geophysics*, *32*(2), 101–195. https://doi.org/10.1007/s10712-010-9104-0

Qian, L., Wang, W., Burns, A. G., Chamberlin, P. C., Coster, A., Zhang, S.-R., & Solomon, S. C. (2019). Solar flare and geomagnetic storm effects on the thermosphere and ionosphere during 6-11 September 2017. *Journal of Geophysical Research: Space Physics*, *124*(3), 2298–2311. https://doi.org/10.1029/2018JA026175

Rideout, W., & Coster, A. (2006). Automated GPS processing for global total electron content data. *GPS Solutions*, *10*(3), 219–228. https://doi.org/10.1007/s10291-006-0029-5

Savitzky, A., & Golay, M. J. E. (1964). Smoothing and differentiation of data by simplified least squares procedures. *Analytical Chemistry*, *36*(8), 1627–1639. https://doi.org/10.1021/ac60214a047

Scherliess, L., & Fejer, B. G. (1997). Storm time dependence of equatorial disturbance dynamo zonal electric fields. *Journal of Geophysical Research*, *102*(A11), 24037–24046. https://doi.org/10.1029/97JA02165

Shiokawa, K., Otsuka, Y., Ogawa, T., & Wilkinson, P. (2004). Time evolution of high-altitude plasma bubbles imaged at geomagnetic conjugate points. *Annales Geophysicae*, *22*(9), 3137–3143. https://doi.org/10.5194/angeo-22-3137-2004

Singh, R., & Sripathi, S. (2017). Ionospheric response to 22-23 June 2015 storm as investigated using ground-based ionosondes and GPS receivers over India. *Journal of Geophysical Research: Space Physics*, *122*(11), 11645–11664. https://doi.org/10.1002/2017JA024460

Sousasantos, J., Gomez Socola, J., Rodrigues, F. S., Eastes, R. W., Brum, C. G. M., & Terra, P. (2023). Severe L-band scintillation over low-to-mid latitudes caused by an extreme equatorial plasma bubble: Joint observations from ground-based monitors and GOLD. *Earth Planets and Space*, *75*(1), 41. https://doi.org/10.1186/s40623-023-01797-5

Spogli, L., Sabbagh, D., Regi, M., Cesaroni, C., Perrone, L., Alfonsi, L., et al. (2021). Ionospheric response over Brazil to the August 2018 geomagnetic storm as probed by CSES 01 and Swarm satellites and by local ground based observations. *Journal of Geophysical Research: Space Physics*, *126*(2), e28368. https://doi.org/10.1029/2020JA028368

Sreeja, V., Ravindran, S., Pant, T. K., Devasia, C. V., & Paxton, L. J. (2009). Equatorial and low-latitude ionosphere-thermosphere system response to the space weather event of August 2005. *Journal of Geophysical Research*, *114*(A12), A12307. https://doi.org/10.1029/2009JA014491

Strickland, D. J., Evans, J. S., & Paxton, L. J. (1995). Satellite remote sensing of thermospheric O/N_2 and solar EUV. 1. Theory. *Journal of Geophysical Research*, *100*(A7), 12217–12226. https://doi.org/10.1029/95JA00574

Sultan, P. J. (1996). Linear theory and modeling of the Rayleigh-Taylor instability leading to the occurrence of equatorial spread F. *Journal of Geophysical Research*, *101*(A12), 26875–26892. https://doi.org/10.1029/96JA00682

Thomas, E. G., Baker, J. B. H., Ruohoniemi, J. M., Clausen, L. B. N., Coster, A. J., Foster, J. C., & Erickson, P. J. (2013). Direct observations of the role of convection electric field in the formation of a polar tongue of ionization from storm enhanced density. *Journal of Geophysical Research: Space Physics*, *118*(3), 1180–1189. https://doi.org/10.1002/jgra.50116

Tsurutani, B., Mannucci, A., Iijima, B., Abdu, M. A., Sobral, J. H. A., Gonzalez, W., & Vasyliunas, V. M. (2004). Global dayside ionospheric uplift and enhancement associated with interplanetary electric fields. *Journal of Geophysical Research*, *109*(A8), A08302. https://doi.org/10.1029/2003JA010342

Tsurutani, B., Verkhoglyadova, O. P., Mannucci, A. J., Saito, A., Araki, T., Yumoto, K., et al. (2008). Prompt penetration electric fields (PPEFs) and their ionospheric effects during the great magnetic storm of 30-31 October 2003. *Journal of Geophysical Research*, *113*(A5), A05311. https://doi.org/10.1029/2007JA012879

Tulasi Ram, S., Rama Rao, P. V. S., Prasad, D. S. V. V. D., Niranjan, K., Gopi Krishna, S., Sridharan, R., & Ravindran, S. (2008). Local time dependent response of postsunset ESF during geomagnetic storms. *Journal of Geophysical Research*, *113*(A7), A07310. https://doi.org/10.1029/2007JA012922

Vierinen, J., Coster, A. J., Rideout, W. C., Erickson, P. J., & Norberg, J. (2016). Statistical framework for estimating GNSS bias. *Atmospheric Measurement Techniques*, *9*(3), 1303–1312. https://doi.org/10.5194/amt-9-1303-2016

Wang, W., Burns, A. G., & Liu, J. (2021). Upper thermospheric winds. In *Upper atmosphere dynamics and energetics* (pp. 41–63). American Geophysical Union. https://doi.org/10.1002/9781119815631.ch3

Wang, W., Talaat, E. R., Burns, A. G., Emery, B., Hsieh, S.-Y., Lei, J., & Xu, J. (2012). Thermosphere and ionosphere response to subauroral polarization streams (SAPS): Model simulations. *Journal of Geophysical Research*, *117*(A7), A07301. https://doi.org/10.1029/2012JA017656

Wang, Z., Zou, S., Liu, L., Ren, J., & Aa, E. (2021). Hemispheric asymmetries in the mid latitude ionosphere during the September 7-8, 2017 storm: Multi instrument observations. *Journal of Geophysical Research: Space Physics*, *126*(4), e28829. https://doi.org/10.1029/2020JA028829

Woodman, R. F., & La Hoz, C. (1976). Radar observations of F region equatorial irregularities. *Journal of Geophysical Research*, *81*(A31), 5447–5466. https://doi.org/10.1029/JA081i031p05447

Yeh, H. C., Su, S. Y., & Heelis, R. A. (2001). Storm time plasma irregularities in the pre-dawn hours observed by the low-latitude ROCSAT-1 satellite at 600 km altitude. *Geophysical Research Letters*, *28*(4), 685–688. https://doi.org/10.1029/2000GL012183

Yizengaw, E., Moldwin, M. B., & Galvan, D. A. (2006). Ionospheric signatures of a plasmaspheric plume over Europe. *Geophysical Research Letters*, *33*(17), L17103. https://doi.org/10.1029/2006GL026597

Zakharenkova, I., & Cherniak, I. (2020). When plasma streams tie up equatorial plasma irregularities with auroral ones. *Space Weather*, *18*(2), e02375. https://doi.org/10.1029/2019SW002375

Zakharenkova, I., Cherniak, I., & Krankowski, A. (2019). Features of storm-induced ionospheric irregularities from ground-based and spaceborne GPS observations during the 2015 St. Patrick's day storm. *Journal of Geophysical Research: Space Physics*, *124*(12), 10728–10748. https://doi.org/10.1029/2019JA026782

Zhai, C., Cai, X., Wang, W., Coster, A., Qian, L., Solomon, S. C., et al. (2023). Mid-latitude ionospheric response to a weak geomagnetic activity event during solar minimum. *Journal of Geophysical Research: Space Physics*, *128*(1), e2022JA030908. https://doi.org/10.1029/2022JA030908

Zhang, S.-R., & Aa, E. (2021). Ionospheric electron density large gradients at midlatitudes. In Y. Nishimura, O. Verkhoglyadova, Y. Deng, & S.-R. Zhang (Eds.), *Cross-scale coupling and energy transfer in the magnetosphere-ionosphere-thermosphere system* (pp. 175–193). Elsevier.

Zhang, S.-R., Erickson, P. J., Coster, A. J., Rideout, W., Vierinen, J., Jonah, O., & Goncharenko, L. P. (2019). Subauroral and polar traveling ionospheric disturbances during the 7-9 September 2017 storms. *Space Weather*, *17*(12), 1748–1764. https://doi.org/10.1029/2019SW002325

Zhang, S.-R., Erickson, P. J., Zhang, Y., Wang, W., Huang, C., Coster, A. J., et al. (2017). Observations of ion-neutral coupling associated with strong electrodynamic disturbances during the 2015 St. Patrick's day storm. *Journal of Geophysical Research: Space Physics*, *122*(1), 1314–1337. https://doi.org/10.1002/2016JA023307

Zhang, S.-R., Nishimura, Y., Erickson, P. J., Aa, E., Kil, H., Deng, Y., et al. (2022). Traveling ionospheric disturbances in the vicinity of storm-enhanced density at midlatitudes. *Journal of Geophysical Research: Space Physics*, *127*(8), e30429. https://doi.org/10.1029/2022JA030429

Zhao, B., Wan, W., & Liu, L. (2005). Responses of equatorial anomaly to the October-November 2003 superstorms. *Annales Geophysicae*, *23*(3), 693–706. https://doi.org/10.5194/angeo-23-693-2005

Zou, S., Moldwin, M. B., Ridley, A. J., Nicolls, M. J., Coster, A. J., Thomas, E. G., & Ruohoniemi, J. M. (2014). On the generation/decay of the storm-enhanced density plumes: Role of the convection flow and field-aligned ion flow. *Journal of Geophysical Research: Space Physics*, *119*(10), 8543–8559. https://doi.org/10.1002/2014JA020408

Zou, S., Ridley, A. J., Moldwin, M. B., Nicolls, M. J., Coster, A. J., Thomas, E. G., & Ruohoniemi, J. M. (2013). Multi-instrument observations of SED during 24-25 October 2011 storm: Implications for SED formation processes. *Journal of Geophysical Research: Space Physics*, *118*(12), 7798–7809. https://doi.org/10.1002/2013JA018860